GEOPHYSICS®

Inversion algorithm determining sharp boundaries in electrical resistivity tomography

Journal:	*Geophysics*
Manuscript ID	GEO-2024-0385.R3
Manuscript Type:	Frontiers in electromagnetic geophysics
Keywords:	resistivity, near surface, electrical/resistivity, electromagnetics, edge detection
Manuscript Focus Area:	Electrical and Electromagnetic Methods, Geophysical Software and Algorithms

SCHOLARONE™
Manuscripts

Downloaded 02/13/25 to 130.54.130.252. Redistribution subject to SEG license or copyright; see Terms of Use at http://library.seg.org/page/policies/terms
DOI:10.1190/geo2024-0385.1

This paper presented here as accepted for publication in Geophysics prior to copyediting and composition.
© 2025 The Authors. Published by the Society of Exploration Geophysicists.

Inversion algorithm determining sharp boundaries in electrical resistivity tomography

Keiichi Ishizu*[1,2,6], Tada-nori Goto[2], Yukitoshi Fukahata[3], Katsuaki Koike[1], Chatchai Vachiratienchai[4], and Weerachai Siripunvaraporn[5]

[1]Graduate School of Engineering, Kyoto University, Katsura, Nisikyo-ku, Kyoto 615-8540, Japan

[2]Graduate School of Science, University of Hyogo, Shosha, Himeji, Hyogo 671-2280, Japan

[3]Disaster Prevention Research Institute, Kyoto University, Gokaho, Uji, Kyoto, 611-0011, Japan

[4]Curl-E Geophysics Co., Ltd., Nakhon Pathom 73170, Thailand

[5]Department of Physics, Faculty of Science, Mahidol University, Bangkok, 10400, Thailand

[6]Now at Department of Earth Resources Engineering, Kyushu University, Fukuoka, 819-0395, Japan.

*Corresponding author: Keiichi Ishizu

Running head: Inversion delineating sharp boundaries

Original paper date of submission: 10 June 2024

ABSTRACT

Blurred resistivity boundaries resulting from smoothness-regularized inversions of electrical resistivity tomography (ERT) data can lead to inaccurate interpretations of sharp

Downloaded 02/13/25 to 130.54.130.252. Redistribution subject to SEG license or copyright; see Terms of Use at http://library.seg.org/page/policies/terms
DOI:10.1190/geo2024-0365.1

This paper presented here as accepted for publication in Geophysics prior to copyediting and composition.
© 2025 The Authors. Published by the Society of Exploration Geophysicists.

boundary structures. To address this issue, various ERT inversion algorithms have introduced localized adjustments (localized discontinuities) in the regularization operator at positions where sharp boundaries are anticipated. Current approaches rely on prior information about sharp boundary locations, obtained from complementary geophysical, geological, and drilling data, to determine the positions and weights for these regularization adjustments. However, such prior information is frequently insufficient, limiting the application of localized regularization adjustments. Accordingly, we developed a sharp boundary inversion (SBI) algorithm using the Akaike Bayesian Information Criterion (ABIC) that determines the optimal positions and weights for localized regularization adjustments by testing various configurations and selecting the one that minimizes ABIC. A synthetic modeling study demonstrated that the SBI algorithm correctly delineated the sharp boundaries of a conductor. Its application to field data demonstrated that it delineated the sharp boundaries of a utility tunnel, and the size and horizontal position of the recovered tunnel were consistent with the estimated dimensions from the blueprint. As it does not rely heavily on prior information, the SBI algorithm can be applied to a wide range of geophysical survey data, even when prior knowledge of sharp boundary locations is limited.

INTRODUCTION

Electrical resistivity tomography (ERT), or electrical resistivity surveys, are used to determine subsurface resistivity structures by measuring the electrical potential generated by direct current sources (Revil et al., 2010; Dahlin and Loke, 2018; Binley and Slater, 2020). As resistivity strongly depends on the existence of fluids, clays, and metals, ERT has been used for investigating soil properties (André et al., 2012), groundwater (Asaue et al., 2021), seawater

Downloaded 02/13/25 to 130.54.130.252. Redistribution subject to SEG license or copyright; see Terms of Use at http://library.seg.org/page/policies/terms
DOI:10.1190/geo2024-0365.1

© 2025 The Authors. Published by the Society of Exploration Geophysicists.

intrusion (Misonou et al., 2013), landfills (Chambers et al., 2006), hydrothermal systems (Gresse et al., 2017), volcanic structures (Soueid Ahmed et al., 2018), landslides (Lapenna et al., 2005), and cavities (Satitpittakul et al., 2013). Other relevant applications include investigating geological structures below lakes (Wang et al., 2018), gas hydrates (Goto et al., 2008; Ishizu et al., 2024a), and massive sulfide deposits in marine environments (Ishizu et al., 2019b).

ERT data are inverted to obtain resistivity structures (Sasaki, 1994; Kemna et al., 2002; Günther et al., 2006). Common ERT inversions find resistivity structures by minimizing the misfit between the measured and modeled data (Amatyakul et al., 2017; Binley and Slater, 2020). As ERT data inversion is an ill-posed problem, regularization terms imposing smoothness constraints are applied to stabilize the solutions (Constable et al., 1987). Smoothness-regularized inversions effectively recover smoothly distributed structures.

However, smoothness-based inversions cannot resolve the sharp resistivity boundaries (Loke et al., 2003). This limitation hinders the investigation of sharp boundary structures such as man-made structures (Hung et al., 2022), faults (Rizzo et al., 2004), and metal deposits (Ishizu et al., 2019b) because the blurred boundaries can lead to mispositioning of these structures. Therefore, recovering sharp resistivity boundaries is essential for accurately assessing the positions and properties of these structures.

Various approaches have been applied to the inversion of ERT and electromagnetic data to recover sharp resistivity boundaries. One approach involves applying localized adjustments (small weight) to the L2-norm smoothness regularization term at positions where sharp boundaries are predicted (Slater and Binley, 2006; Key, 2009). This approach is highly sensitive to the accuracy of prior information about sharp boundary locations (Hermans et al., 2012; Johnson et al., 2012; Zhou et al., 2014). Other inversion approaches use sparse

Downloaded 02/13/25 to 130.54.130.252. Redistribution subject to SEG license or copyright; see Terms of Use at http://library.seg.org/page/policies/terms
DOI:10.1190/geo2024-0365.1

This paper presented here as accepted for publication in Geophysics prior to copyediting and composition.
© 2025 The Authors. Published by the Society of Exploration Geophysicists.

regularizations, such as minimum gradient support regularization and L1-norm regularization, to recover sharp resistivity boundaries (Farquharson, 2008; Vignoli et al., 2015; Klose et al., 2022; Deleersnyder et al., 2023). These approaches do not necessarily require prior information on sharp boundary positions; instead, the selection of additional parameters is needed to control the sharpness of the model structure. In this study, we employ localized adjustments to the L2-norm regularization term, as we assume that structures other than those with sharp boundaries exhibit a smooth resistivity distribution.

Previous studies have determined the positions and weights of localized regularization adjustments from prior information on sharp boundary locations estimated from other geophysical, geological, and drilling data (Hermans et al., 2012; Johnson et al., 2012; Zhou et al., 2014). For instance, Johnson et al. (2012) used geological data and borehole resistivity data to determine the positions and weights of localized regularization adjustments. Doetsch et al. (2012) and Zhou et al. (2014) used subsurface structural information obtained from ground-penetrating radar images to determine the positions and weights. However, prior information on sharp boundary locations is often inadequate, causing the limited application of this approach. Therefore, an inversion algorithm that determines the correct positions and optimal weights for localized regularization adjustments from insufficient prior information is necessary. Accordingly, this study developed a sharp boundary inversion (SBI) algorithm using the Akaike Bayesian Information Criterion (ABIC) which favors models with higher likelihood and entropy (Akaike, 1980) to determine the correct positions and optimal weights of localized regularization adjustments from insufficient prior information .

The ABIC has been applied to inversion algorithms of various geophysical data for linear problems, such as geodetic data (Yabuki and Matsu’ura, 1992; Fukahata et al., 2004) and

Downloaded 02/13/25 to 130.54.130.252. Redistribution subject to SEG license or copyright; see Terms of Use at http://library.seg.org/page/policies/terms
DOI:10.1190/geo2024-0365.1

This paper presented here as accepted for publication in Geophysics prior to copyediting and composition.
© 2025 The Authors. Published by the Society of Exploration Geophysicists.

nonlinear problems, such as Interferometric Synthetic Aperture Radar (Fukahata and Hashimoto, 2016), ERT (Uchida, 1993a), magnetotelluric (Uchida, 1993b; Ogawa and Uchida, 1996), and controlled source electromagnetic data (Mitsuhata et al., 2002) to determine the optimal tradeoff parameters of model regularization and data misfit terms. Moreover, to recover sharp boundaries at fixed positions in magnetotelluric inversion, Kimura et al. (2010) used ABIC to determine the weights for localized adjustments in the smoothness regularization. Our SBI newly extends the ABIC application to determine both the positions and weights for localized regularization adjustments and the tradeoff parameter.

This study aimed to develop an SBI algorithm that is applicable even when prior information on sharp boundary locations is limited and demonstrate its effectiveness using synthetic and field data. We first describe the SBI algorithm. Next, we used a synthetic dataset from a two-dimensional (2D) ERT survey and demonstrate the effectiveness of the SBI algorithm by comparing the true boundaries of a rectangular anomaly with those determined by the SBI algorithm. We applied the SBI algorithm to a field dataset to investigate a utility tunnel with sharp rectangular boundaries. Comparing the size and horizontal location of the tunnel determined by the SBI algorithm with those estimated from the blueprint demonstrated its effectiveness.

METHOD

We first describe the incorporation of ABIC into an ERT inversion. Then, we explain the SBI algorithm using ABIC.

Incorporating ABIC into inversion with localized regularization adjustments

Downloaded 02/13/25 to 130.54.130.252. Redistribution subject to SEG license or copyright; see Terms of Use at http://library.seg.org/page/policies/terms
DOI:10.1190/geo2024-0365.1

This paper presented here as accepted for publication in Geophysics prior to copyediting and composition.
© 2025 The Authors. Published by the Society of Exploration Geophysicists.

Although previous studies have used ABIC only to determine tradeoff parameters (Uchida, 1993a; Mitsuhata et al., 2002; Fukahata et al., 2004), we incorporated ABIC into an ERT inversion to determine both the positions and weights for the localized regularization adjustments and the tradeoff parameter. We modified an Occam-algorithm inversion code for ERT data developed by Ishizu et al. (2019a), using a finite difference forward solver with rectangular elements, to apply the ABIC.

The data misfit term $S[\mathbf{m}]$ of the ERT inversion is defined as follows (Constable et al., 1987):

$$S[\mathbf{m}] = \|\mathbf{W}(\mathbf{d} - \mathbf{F}[\mathbf{m}])\|^2 (1)$$

where $\mathbf{d}$ is a vector of measured apparent resistivity data, $\mathbf{F}[\mathbf{m}]$ is a vector of the forward modeled response from the conductivity model $\mathbf{m}$, and $\mathbf{W}$ represents the data weight matrix with diagonal element equal to $\mathbf{W}_{ii} = 1/\varepsilon_i$ where ε_i is the error level of the ith data point. The dimensions of $\mathbf{d}$ and $\mathbf{m}$ are N and M, respectively. We applied natural log transformation to the apparent resistivity data of $\mathbf{d}$ and the conductivity model of $\mathbf{m}$ (Vachiratienchai and Siripunvaraporn, 2013).

Obtaining the model by minimizing equation 1 is an ill-posed problem for ERT data. We stabilized the solution of equation 1 with the L2-norm model regularization term

$$R[\mathbf{m}] = \|\mathbf{C}\mathbf{m}\|^2 (2)$$

where $\mathbf{C}$ is the weighted first-derivative roughness operator described as

$$\mathbf{C} = \mathbf{W}_x\mathbf{R}_x + \mathbf{W}_z\mathbf{R}_z (3)$$

where $\mathbf{R}_x$ and $\mathbf{R}_z$ are the first-derivative roughness operators in the x and z directions, respectively, and $\mathbf{W}_x$ and $\mathbf{W}_z$ represent weights applied to $\mathbf{R}_x$ and $\mathbf{R}_z$, respectively. Localized regularization adjustments (localized discontinuities) can be applied to recover sharp boundaries

Downloaded 02/13/25 to 130.54.130.252. Redistribution subject to SEG license or copyright; see Terms of Use at http://library.seg.org/page/policies/terms
DOI:10.1190/geo2024-0365.1

This paper presented here as accepted for publication in Geophysics prior to copyediting and composition.
© 2025 The Authors. Published by the Society of Exploration Geophysicists.

by setting small weights in $\mathbf{W}_x$ and $\mathbf{W}_z$ at the boundaries (Key, 2009; Johnson et al., 2012). To describe $\mathbf{C}$, we considered a five-layered model in the *z*-direction as a simplified representation. $\mathbf{W}_z\mathbf{R}_z$ is then expressed as

$$\mathbf{W}_z\mathbf{R}_z = \begin{bmatrix} w_{z1} & 0 & 0 & 0 & 0 \\ 0 & w_{z2} & 0 & 0 & 0 \\ 0 & 0 & w_{z3} & 0 & 0 \\ 0 & 0 & 0 & w_{z4} & 0 \\ 0 & 0 & 0 & 0 & w_{z5} \end{bmatrix} \begin{bmatrix} -1 & 1 & 0 & 0 & 0 \\ 0 & -1 & 1 & 0 & 0 \\ 0 & 0 & -1 & 1 & 0 \\ 0 & 0 & 0 & -1 & 1 \\ 0 & 0 & 0 & 0 & q \end{bmatrix} (4)$$

The values of w_{z1}–w_{z5} were set to one, except for the positions where localized adjustments were applied. If a localized adjustment was used between the second and third layers, the SBI algorithm applies a small value equal to *bv* (localized discontinuity parameter) in w_{z2}. The regularization term $R[\mathbf{m}]$, tuned with an appropriate parameter *bv*, enables the recovery of sharp boundaries. To satisfy the full-rank condition required for ABIC applications (Fukahata, 2012), we constrained the minimum value of *bv* to 10^{-4}. The SBI algorithm determined the optimal *bv* by minimizing ABIC. Another small value of *q* was applied to the end of the layered model to satisfy the full-rank condition. We set *q* to 10^{-2} because it satisfies the full-rank condition but does not affect inversion results. Although we present the five-layered model to illustrate $\mathbf{C}$, we extended this conceptual framework to a 2D model with dimensions of *M*. In the 2D application, localized regularization adjustments were performed for both $\mathbf{W}_x$ and $\mathbf{W}_z$.

The inversion minimizes the objective function

$$U[\mathbf{m}] = S[\mathbf{m}] + \lambda R[\mathbf{m}] = \|\mathbf{W}(\mathbf{d} - \mathbf{F}[\mathbf{m}])\|^2 + \lambda\|\mathbf{Cm}\|^2 (5)$$

where λ is a tradeoff parameter between data fit and model regularization, referred to as a hyperparameter in the ABIC framework (Akaike, 1980). Alternatively, $U[\mathbf{m}]$ can be expressed as

$$U[\mathbf{m}] = (\mathbf{d} - \mathbf{F}[\mathbf{m}])^{\mathrm{T}}\mathbf{C}_d^{-1}(\mathbf{d} - \mathbf{F}[\mathbf{m}]) + \lambda\mathbf{m}^{\mathrm{T}}\mathbf{C}_m^{-1}\mathbf{m} (6)$$

where

Downloaded 02/13/25 to 130.54.130.252. Redistribution subject to SEG license or copyright; see Terms of Use at http://library.seg.org/page/policies/terms
DOI:10.1190/geo2024-0365.1

This paper presented here as accepted for publication in Geophysics prior to copyediting and composition.
© 2025 The Authors. Published by the Society of Exploration Geophysicists.

$$\mathbf{C}_d^{-1} = \mathbf{W}^{\mathrm{T}}\mathbf{W} \quad (7)$$

and

$$\mathbf{C}_m^{-1} = \mathbf{C}^{\mathrm{T}}\mathbf{C} = (\mathbf{W}_x\mathbf{R}_x)^{\mathrm{T}}\mathbf{W}_x\mathbf{R}_x + (\mathbf{W}_z\mathbf{R}_z)^{\mathrm{T}}\mathbf{W}_z\mathbf{R}_z \quad (8)$$

Owing to the non-linearity of the inversion, we linearized $\mathbf{F}[\mathbf{m}]$ about a model at the kth iteration ($\mathbf{m}_k$) such that

$$\mathbf{F}[\mathbf{m}_{k+1}] = \mathbf{F}[\mathbf{m}_k] + \mathbf{J}_k(\mathbf{m}_{k+1} - \mathbf{m}_k) \quad (9)$$

where $\mathbf{J}_k$ is the $N \times M$ Jacobian matrix. Using equation 9, the linearized objective function U^{L} is expressed as

$$U^{\mathrm{L}}[\mathbf{m}_{k+1}] = \left\|\mathbf{W}\left(\hat{\mathbf{d}}_k - \mathbf{J}_k\mathbf{m}_{k+1}\right)\right\|^2 + \lambda\|\mathbf{C}\mathbf{m}_{k+1}\|^2 \quad (10)$$

where

$$\hat{\mathbf{d}}_k = \mathbf{d} - \mathbf{F}[\mathbf{m}_k] + \mathbf{J}_k\mathbf{m}_k \quad (11)$$

Alternatively, $U^{\mathrm{L}}[\mathbf{m}_{k+1}]$ can be written as

$$U^{\mathrm{L}}[\mathbf{m}_{k+1}] = \left(\hat{\mathbf{d}}_k - \mathbf{J}_k\mathbf{m}_{k+1}\right)^{\mathrm{T}}\mathbf{C}_d^{-1}\left(\hat{\mathbf{d}}_k - \mathbf{J}_k\mathbf{m}_{k+1}\right) + \lambda\mathbf{m}_{k+1}{}^{\mathrm{T}}\mathbf{C}_m^{-1}\mathbf{m}_{k+1} \quad (12)$$

To minimize equation 12 with a fixed λ, the derivative of U^{L} for $\mathbf{m}_{k+1}$ was set to zero, solving the following equation to obtain the optimal solution $\mathbf{m}_{k+1}^*$ such that

$$\left[\lambda\mathbf{C}_m^{-1} + \mathbf{J}_k^{\mathrm{T}}\mathbf{C}_d^{-1}\mathbf{J}_k\right]\mathbf{m}_{k+1}^* = \mathbf{J}_k^{\mathrm{T}}\mathbf{C}_d^{-1}\hat{\mathbf{d}}_k \quad (13)$$

Now, we introduce the ABIC based on the Bayes' theorem (Akaike, 1980). Given that the observed data contain Gaussian noise and relative values of the data covariance matrix $\mathbf{C}_d$ are available, the probability density function of the data with multidimensional normal distribution is written as

$$p(\mathbf{d}|\mathbf{m}_{k+1}) = \left(2\pi\sigma_0^2\right)^{-N/2}|\mathbf{C}_d^{-1}|^{1/2}\exp\left(-\frac{1}{2\sigma_0^2}\left(\hat{\mathbf{d}}_k - \mathbf{J}_k\mathbf{m}_{k+1}\right)^{\mathrm{T}}\mathbf{C}_d^{-1}\left(\hat{\mathbf{d}}_k - \mathbf{J}_k\mathbf{m}_{k+1}\right)\right) \quad (14)$$

Downloaded 02/13/25 to 130.54.130.252. Redistribution subject to SEG license or copyright; see Terms of Use at http://library.seg.org/page/policies/terms
DOI:10.1190/geo2024-0395.1

This paper presented here as accepted for publication in Geophysics prior to copyediting and composition.
© 2025 The Authors. Published by the Society of Exploration Geophysicists.

where σ_0^2 is correction factor of $\mathbf{C}_d$ (Mitsuhata et al., 2002; Fukahata et al., 2004). The probability density function of the *a priori* information on the model parameters is also expressed as

$$p(\mathbf{m}_{k+1}) = \left(2\pi\rho^2\right)^{-M/2}|\mathbf{C}_m^{-1}|^{1/2}\exp\left(-\frac{1}{2\rho^2}\mathbf{m}_{k+1}{}^{\mathrm{T}}\mathbf{C}_m^{-1}\mathbf{m}_{k+1}\right)(15)$$

where ρ^2 represent variances of the *a priori* information. Using Bayes' theorem, the posterior distribution $p(\mathbf{m}_{k+1}|\mathbf{d})$ can be formulated as (Yabuki and Matsu'ura, 1992)

$$p(\mathbf{m}_{k+1}|\mathbf{d}) \propto p(\mathbf{d}|\mathbf{m}_{k+1})p(\mathbf{m}_{k+1}) = \left(2\pi\sigma_0^2\right)^{-N/2}\left(2\pi\sigma_0^2\right)^{-M/2}(\lambda)^{M/2}|\mathbf{C}_d^{-1}|^{1/2}|\mathbf{C}_m^{-1}|^{1/2}\exp\left(-\frac{U^{\mathrm{L}}[\mathbf{m}_{k+1}]}{2\sigma_0^2}\right)(16)$$

and

$$\lambda = \frac{\sigma_0^2}{\rho^2}(17)$$

ABIC is defined as

$$\mathrm{ABIC} = -2\log L + 2N_{\mathrm{P}}(18)$$

where L is the marginal likelihood and N_{P} is the number of hyperparameters (Akaike, 1980). In conventional smoothing inversion, λ is the only hyperparameter ($N_{\mathrm{P}} = 1$). In contrast, the number of hyperparameters for the SBI algorithm varies depending on the number of boundaries for localized regularization adjustments because their positions and weights are themselves hyperparameters determined by ABIC minimization. If the SBI algorithm determines four boundary positions (top, bottom, left, and right sides of a rectangle), their weight (*bv*), and λ, $N_{\mathrm{P}} = 6$. Following Yabuki and Matsu'ura (1992), L is expressed as

$$L = \int p(\mathbf{d}|\mathbf{m}_{k+1})p(\mathbf{m}_{k+1})d\mathbf{m}_{k+1} = \left(2\pi\sigma_0^2\right)^{-N/2}(\lambda)^{M/2}|\mathbf{C}_d^{-1}|^{1/2}|\mathbf{C}_m^{-1}|^{1/2}|\mathbf{J}_k^{\mathrm{T}}\mathbf{C}_d^{-1}\mathbf{J}_k + \lambda\mathbf{C}_m^{-1}|^{-1/2} \times \exp\left(-\frac{U^{\mathrm{L}}[\mathbf{m}_{k+1}^*])}{2\sigma_0^2}\right).$$

(19)

Downloaded 02/13/25 to 130.54.130.252. Redistribution subject to SEG license or copyright; see Terms of Use at http://library.seg.org/page/policies/terms
DOI:10.1190/geo2024-0365.1

This paper presented here as accepted for publication in Geophysics prior to copyediting and composition.
© 2025 The Authors. Published by the Society of Exploration Geophysicists.

To minimize ABIC, we maximize L, which is a function of σ_0^2, λ and $\mathbf{C}_m^{-1}$. The maximum L for σ_0^2 is obtained as $\sigma_0^2 = \frac{U^{\mathrm{L}}[\mathbf{m}_{k+1}^*]}{N}$ by solving $\frac{\partial L}{\partial \sigma_0^2} = 0$. The equations for $\frac{\partial L}{\partial \lambda} = 0$ and $\frac{\partial L}{\partial \mathbf{C}_m^{-1}} = 0$ cannot be solved analytically. We maximize L for λ and $\mathbf{C}_m^{-1}$ using a search algorithm described in the next section. By substituting $\sigma_0^2 = \frac{U^{\mathrm{L}}[\mathbf{m}_{k+1}^*]}{N}$ to equation 19, L is expressed as

$$L = \left(2\pi \frac{U^{\mathrm{L}}[\mathbf{m}_{k+1}^*]}{N}\right)^{-N/2} (\lambda)^{M/2} |\mathbf{C}_d^{-1}|^{1/2} |\mathbf{C}_m^{-1}|^{1/2} |\mathbf{J}_k^{\mathrm{T}} \mathbf{C}_d^{-1} \mathbf{J}_k + \lambda \mathbf{C}_m^{-1}|^{-1/2} \exp\left(-\frac{N}{2}\right) (20)$$

Consequently, the linearized ABIC version ($\mathrm{ABIC}^{\mathrm{L}}$) is defined as

$$\mathrm{ABIC}^{\mathrm{L}}\left(\lambda, \mathbf{C}_m^{-1}\right) = N \log\left(U^{\mathrm{L}}\,[\mathbf{m}_{k+1}^*]\right) - M \log\lambda - \log|\mathbf{C}_m^{-1}| + \log|\mathbf{J}_k^{\mathrm{T}} \mathbf{C}_d^{-1} \mathbf{J}_k + \lambda \mathbf{C}_m^{-1}| + 2N_{\mathrm{P}} + Q (21)$$

where Q is independent of λ and $\mathbf{C}_m^{-1}$. Instead of $\mathrm{ABIC}^{\mathrm{L}}$, we used the quasi-linearized ABIC version of $\mathrm{ABIC}^{\mathrm{QL}}$ (from now on simply called ABIC) to mitigate linearization errors (Mitsuhata et al., 2002) expressed as

$$\mathrm{ABIC}^{\mathrm{QL}}\left(\lambda, \mathbf{C}_m^{-1}\right) = N \log(U\,[\mathbf{m}_{k+1}^*]) - M \log\lambda - \log|\mathbf{C}_m^{-1}| + \log|\mathbf{J}_k^{\mathrm{T}} \mathbf{C}_d^{-1} \mathbf{J}_k + \lambda \mathbf{C}_m^{-1}| + 2N_{\mathrm{P}} + Q, (22)$$

and $U\,[\mathbf{m}_{k+1}^*]$ is computed as

$$U\,[\mathbf{m}_{k+1}^*] = (\mathbf{d} - \mathbf{F}[\mathbf{m}_{k+1}^*])^{\mathrm{T}} \mathbf{C}_d^{-1} (\mathbf{d} - \mathbf{F}[\mathbf{m}_{k+1}^*]) + \lambda {\mathbf{m}_{k+1}^*}^{\mathrm{T}} \mathbf{C}_m^{-1} \mathbf{m}_{k+1}^* (23)$$

ABIC in the SBI algorithm depends on λ and $\mathbf{C}_m^{-1}$ (positions and weights for localized adjustments in the regularization operator), whereas ABIC used in the previous studies depended only on λ (Uchida, 1993a; Mitsuhata et al., 2002).

To evaluate the inversion performance, we considered an L1-norm misfit between the inverted and true models as follows:

$$\text{Model misfit} = \sum_{i=1}^{M} |m_i - m_i^{true}| (24)$$

Downloaded 02/13/25 to 130.54.130.252. Redistribution subject to SEG license or copyright; see Terms of Use at http://library.seg.org/page/policies/terms
DOI:10.1190/geo2024-0365.1

This paper presented here as accepted for publication in Geophysics prior to copyediting and composition.
© 2025 The Authors. Published by the Society of Exploration Geophysicists.

where m_i and m_i^{true} are, respectively, the *i*th conductivity parameters of the inverted and true models. The root-mean-square (rms) data misfit is defined to measure the fit of the model response to the observed data

$$\text{rms data misfit} = \sqrt{\frac{(\mathbf{d}-\mathbf{F}[\mathbf{m}])^{\mathrm{T}}\mathbf{C}_{\mathbf{d}}^{-1}(\mathbf{d}-\mathbf{F}[\mathbf{m}])}{N}}. \quad (25)$$

Algorithm to delineate sharp boundaries using ABIC

The SBI algorithm determined the optimal positions and weights for localized regularization adjustments, assuming *a priori* information about the target structure: a rectangular shape but unknown size or depth. It is summarized as follows (Figure 1). First, we implemented an inversion with conventional smoothness regularization (Flow 1) and located the initial sharp boundaries based on the change in the first derivative of the smooth model (Flow 2). It is computed by applying $\mathbf{R}_x$ and $\mathbf{R}_z$ to the conductivity model of $\mathbf{m}$. The initial sharp boundaries were assigned at positions where the roughness exhibited high values.

In Flow 3, we conducted inversion analyses with localized regularization adjustments and searched for the optimal left and right boundaries by minimizing ABIC through a grid search of the boundary positions, while the top and bottom of the sharp boundaries were fixed to the initial locations determined in Flow 2. Simultaneously, we determined an optimal *bv* by trying various values, ranging from 10^{-4} to one (Flow 3). The same *bv* value was assigned for all the localized regularization adjustments. In Flow 4, the optimal top and bottom boundaries and *bv* were determined, fixing the left and right boundaries determined in Flow 3. Finally, the model with the minimum ABIC in Flow 4 was selected as optimal. Note that in each inversion run, we also

Downloaded 02/13/25 to 130.54.130.252. Redistribution subject to SEG license or copyright; see Terms of Use at http://library.seg.org/page/policies/terms
DOI:10.1190/geo2024-0365.1

This paper presented here as accepted for publication in Geophysics prior to copyediting and composition.
© 2025 The Authors. Published by the Society of Exploration Geophysicists.

Downloaded 02/13/25 to 130.54.130.252. Redistribution subject to SEG license or copyright; see Terms of Use at http://library.seg.org/page/policies/terms
DOI:10.1190/geo2024-0365.1

searched for the optimal λ that minimized ABIC using forty log10-scaled trial λ values with a 0.1 spacing.

RESULTS AND DISCUSSION

Synthetic modeling study for a rectangular structure

A synthetic ERT dataset was generated using the test model (Figure 2). The survey employed a dipole-dipole configuration with a 2 m electrode spacing over a 54-m long profile on a flat ground, resulting in N = 172 apparent resistivity data points. The test model included a 10-Ωm conductor with sharp rectangular boundaries (x = 20–26 m and z = 1.5–6 m) embedded in a 100-Ωm homogeneous half-space structure. The apparent resistivity data were computed via forward modeling, and 2% Gaussian noise was added. A 2% error level was applied to all data, namely $\varepsilon_i = 0.02 \times |d_i|$ for i = 1, …, N. The model was discretized into 74 × 21 cells in the x- and z-directions, resulting in M = 1554. A grid spacing of 1 m was used horizontally (x-direction: 0 to 54 m). Vertically (z-direction), a finer spacing of 0.5 m was used for the upper 2 m, and a coarser spacing of 1 m was used for depths between 2 and 10 m. The grid size was gradually increased to the boundary positions in the x- and z-directions. A 100-Ωm initial model was used for all synthetic data inversions. The data and model settings were chosen based on existing field data.

The SBI algorithm started with a conventional smoothing inversion (no localized regularization adjustments). The smoothing inversion converged after four iterations and recovered a conductor with blurred outlines (Flow 1; Figure 3a). The ABIC value in equation 22 and rms data misfit in equation 25 for the smooth model were 1322.5 and 0.73, respectively. Initial boundaries were suggested to be located at x = 20 m, x = 26 m, z = 1.5 m, and z = 5 m

This paper presented here as accepted for publication in Geophysics prior to copyediting and composition.
© 2025 The Authors. Published by the Society of Exploration Geophysicists.

based on the maximum rate of change in the first derivative of the smooth model, while the true boundaries were $x = 20$, $x = 26$ m, $z = 1.5$, and $z = 6$ m (Flow 2; Figures 3b and 3c). The initial boundaries were quite close to the true model boundaries. To enhance the realism of the test, we used slightly shifted initial boundaries of $x = 19$, $x = 27$ m, $z = 1$ m, and $z = 7$ m.

In Flow 3, we first implemented the inversion using localized regularization adjustments for the initial locations of $x = 19$ m, $x = 27$ m, $z = 1$ m, and $z = 7$ m. The inversion with $bv = 10^{-2}$ yielded an ABIC value of 1270.7 and a rms data misfit of 0.83 (Figure 4a). Although the ABIC was lower than that of the smoothness inversion, the outline of the recovered conductor was still blurred because of incorrect positions for the localized discontinuity. In the Flow 3, we estimated the correct left and right boundaries ($x = 20$ m and $x = 26$ m) with $bv = 10^{-2}$ (Figure 4b) and obtained a model with an ABIC of 1186.5 and a rms data misfit of 0.88. After fixing the left and right boundaries at $x = 20$ m and $x = 26$ m based on Flow 3, we optimized the top and bottom boundaries to minimize the ABIC value (Flow 4). The inversion with the correct top and bottom boundaries ($z = 1.5$ m and $z = 6$ m) with $bv = 10^{-3}$ obtained the optimal model with the minimum ABIC value of 978.3 and a rms data misfit of 1.04 (Figure 4c). The model misfit in equation 24 for the optimal model was 9.2, significantly lower than the conventional smoothness inversion result of 164.2. These results demonstrate that the SBI algorithm effectively determines the correct positions and appropriate weights for localized regularization adjustments and delineates sharp boundaries.

The inversion results revealed several features. The optimal bv value was found to be 10^{-3}, but the ABIC value was relatively insensitive to bv within the range of 10^{-2} to 10^{-4}, indicating that a localized search for bv could be avoided (Figure A1). The lowest ABIC values were obtained with the largest λ (Figures 4 and A1), indicating that the model regularization with

Downloaded 02/13/25 to 130.54.130.252. Redistribution subject to SEG license or copyright; see Terms of Use at http://library.seg.org/page/policies/terms
DOI:10.1190/geo2024-0365.1

This paper presented here as accepted for publication in Geophysics prior to copyediting and composition.
© 2025 The Authors. Published by the Society of Exploration Geophysicists.

Downloaded 02/13/25 to 130.54.130.252. Redistribution subject to SEG license or copyright; see Terms of Use at http://library.seg.org/page/policies/terms
DOI:10.1190/geo2024-0365.1

the given localized discontinuities (Figure 4c) is strongly consistent with the true model consisting of two homogeneous domains of 10 Ωm and 100 Ωm, except for the sharp boundaries. Figure 5 presents cross-plots of ABIC as a function of the left boundary positions, rms misfits, λ, and bv. The smallest ABIC was achieved at the true left boundary position x = 20 m, with the largest λ and largest rms misfit (Figure 5a and 5b), and the smallest bv (Figure 5c). As the boundary position deviated from the true position, λ diminished and the rms misfit slightly decreased, while bv increased, resulting in a larger ABIC value. The inversion utilizing the correct boundary prioritized the regularization term over the data misfit term, resulting in the smallest ABIC value with the largest λ, the largest rms misfit, and the smallest bv. Figure 6 illustrates the variation of the ABIC and rms misfit with respect to the left boundary location, λ, and bv. For each inversion result, the λ minimizing the ABIC exceeds that minimizing the rms misfit. This difference is especially pronounced for the correct left boundary of 20 m with $bv = 10^{-3}$ (Figure 6d). Additionally, with the correct boundary location, the rms misfit increases gradually with λ (Figure 6d), reflecting the consistency between the model regularization and the inverted model.

In the above inversions, the model discretization for inversion perfectly matched the outlines of the true conductor; however, discretization errors commonly occur. The SBI algorithm was applied to a scenario where the vertical grid closest to the true top boundary at z = 1.5 m was shifted between 1.1 m and 1.9 m. The model discretization for the left, right, and bottom boundaries remained consistent with those of the true conductor. The SBI algorithm produced models with ABIC values of 1124.8 and 1136.8 for the vertical grids of 1.2 m and 1.8 m, respectively (Figure 7a and 7b). ABIC values increased as the grid deviated from 1.5 m (Figure 7c), resulting in a minimum ABIC of 978.3 for the correct vertical grid of 1.5 m (Figure

This paper presented here as accepted for publication in Geophysics prior to copyediting and composition.
© 2025 The Authors. Published by the Society of Exploration Geophysicists.

4c). This finding indicates that the SBI algorithm can also optimize the model discretization for sharp boundaries.

Application to field data with a rectangular structure

A field ERT dataset was collected along a flat promenade on a Kyoto University campus using a Super Sting R8 instrument (Advanced Geosciences Inc., Texas, USA) on October 26, 2017. During the ERT survey, we used a dipole-dipole configuration with 2 m electrode spacing over a 54-m profile, obtaining $N = 172$ data points (Figure 8). The target was a utility tunnel with sharp rectangular boundaries. Its size and horizontal position were determined from an existing blueprint, with a horizontal width of 3.5 m, vertical thickness of 4.4 m, and a center at $x = 14$ m. The blueprint also indicates a depth of less than 4.5 m for the tunnel's top, but the exact depth remains unknown. The tunnel frame, made of reinforced concrete, exhibits lower resistivity than the surrounding soil. In contrast, a cavity with effective infinite resistivity is present within the tunnel. Borehole surveys conducted near the ERT profile indicated that the survey area contains sand and clay layers from the surface to a depth of 4.6 m (Kyoto Prefecture Office, 2005). Sedimentary rocks primarily made of shale are distributed below 4.6 m (Kyoto Prefecture Office, 2005). The weather was sunny during the survey, with precipitation occurring before the survey date. The Automated Meteorological Data Acquisition System reported an accumulated precipitation of 182 mm in Kyoto over the five days preceding the survey. These meteorological conditions resulted in elevated moisture levels near the surface, lowering the resistivity than what is typically observed during dry intervals.

The observed apparent resistivity data revealed a low resistivity zone of 10–40 Ωm between $x = 10$ and $x = 20$ m (Figure 9a). This low resistivity zone corresponded to the

Downloaded 02/13/25 to 130.54.130.252. Redistribution subject to SEG license or copyright; see Terms of Use at http://library.seg.org/page/policies/terms
DOI:10.1190/geo2024-0365.1

This paper presented here as accepted for publication in Geophysics prior to copyediting and composition.
© 2025 The Authors. Published by the Society of Exploration Geophysicists.

conductive feature associated with the tunnel. A 100-Ωm initial model was used for all field data inversions. A 2-% error level was applied to all data. Model discretization was the same as that used in the earlier synthetic model.

The SBI algorithm started with the smoothing inversion and converged after three iterations, recovering a conductor with blurred outlines, an ABIC value of 1488.2, and a rms data misfit equal to 1.76 (Flow 1; Figure 9b). The recovered conductor was consistent with the low apparent resistivity data. The change in the first derivative of the smooth model provided an initial location of sharp boundaries as a rectangular shape at x = 11 m, x = 17 m, z = 1.5 m, and z = 7 m (Flow 2; Figure 9c and 9d). In Flow 3, we first implemented the inversion using localized regularization adjustments for the initial location of x = 11 m and x = 17 m; z = 1.5 m and z = 7 m; the inversion with $bv = 10^{-1}$ obtained an ABIC of 1471.1 and rms data misfit of 1.82 (Figure 10a). Then, Flow 3 specified the left and right boundaries as x = 12 m and x = 16 m with $bv = 10^{-1}$, fixing the top and bottom at the initial location as z = 1.5 m and z = 7 m (Figure 10b), the ABIC was 1461.1, and a rms data misfit was 1.78. While the left and right boundaries were fixed at x = 12 m and x = 16 m, Flow 4 specified the top and bottom of the sharp boundaries of z = 2 m and z = 7 m, respectively, with a minimum ABIC of 1449.8 and rms data misfit of 1.80 (Figure 10c).

The size of the tunnel determined by the SBI algorithm (Figure 10c; horizontal width of 4 m, x = 12–16 m; vertical thickness of 5 m, z = 2–7 m) was consistent with the estimated size based on the blueprint (horizontal width of 3.5 m; vertical thickness of 4.4 m). The horizontal location determined using the SBI algorithm (x = 12 and x = 16 m) aligned with the estimated location (x = 12.25 and x = 15.75 m). Furthermore, the resistivity values of the tunnel shown in Figure 10c demonstrated greater uniformity than those presented in Figures 9b and 10a–10b.

Downloaded 02/13/25 to 130.54.130.252. Redistribution subject to SEG license or copyright; see Terms of Use at http://library.seg.org/page/policies/terms
DOI:10.1190/geo2024-0365.1

This paper presented here as accepted for publication in Geophysics prior to copyediting and composition.
© 2025 The Authors. Published by the Society of Exploration Geophysicists.

Given that the tunnel is an engineered structure, it is expected to display a uniform resistivity value. Therefore, the tunnel resistivity values in Figure 10c are deemed accurate in reflecting this characteristic. The cavity inside the tunnel exhibits an infinite resistivity value. However, the influence of the cavity on the ERT data was masked by the surrounding low-resistivity framework owing to the limited resolution of the ERT data. Consequently, the tunnel was imaged as an entity with overall low resistivity. These results proved that the developed SBI algorithm effectively delineated the sharp boundaries of the tunnel. We infer that the slight size deviation resulted from the survey line being aligned diagonally to the tunnel.

Synthetic modeling study for non-rectangular structures

The SBI algorithm was applied to a rectangular target, assuming that the target shape was rectangular. However, prior information on the target shape is often unavailable. In this section, we applied the SBI algorithm to a synthetic dataset generated from a model containing triangular structures, assuming that the structures were rectangular. The purpose of this test was to demonstrate the limitations of the current approach and its potential for broader applicability to complex structures. The test model included two 10 Ωm triangular structures with upward and downward orientations (A1 and A2), embedded in a 100-Ωm homogeneous half-space structure (Figure 11a). The triangular structures had a 9-m base, and were 5 m in height and buried at 1 m depth at the top. The survey array, noise level, and model discretization were similar to those used in the previous two models.

The SBI algorithm started with a smoothing inversion for the synthetic data. The inversion produced a smooth model with an ABIC value of 1409.0 and a rms data misfit of 0.72 (Figure 11b). By assuming that the conductors were rectangular with sharp boundaries, we

Downloaded 02/13/25 to 130.54.130.252. Redistribution subject to SEG license or copyright; see Terms of Use at http://library.seg.org/page/policies/terms
DOI:10.1190/geo2024-0365.1

This paper presented here as accepted for publication in Geophysics prior to copyediting and composition.
© 2025 The Authors. Published by the Society of Exploration Geophysicists.

identified initial sharp boundaries based on the high derivatives of the smooth model. Initial sharp boundary locations are selected at x = 13 m, x =16 m, z = 1.5 m, and z = 7 for A1, and x = 30 m, x =39 m, z = 1 m, and z = 4 m for A2 (light blue lines in Figure 11c and 11d).

The SBI algorithm applied to A1 with $bv = 10^{-1}$ yielded a model with an ABIC value equal to 1394.4 and a rms data misfit of 0.74 after Flow 4 (Figure 12a). The SBI algorithm applied to A2 with $bv = 10^{-1}$ resulted in a model with an ABIC of 1366.2 and rms data misfit of 0.77 after Flow 4 (Figure 12b). The SBI algorithm applied to A1 and A2 with $bv = 10^{-2}$ produced a model with an ABIC of 1277.2 and rms data misfit of 0.95 after Flow 4 (Figure 12c). The boundaries of A1 and A2 were not correctly recovered in these models (Figure 12a–12c) except for the top boundary of A2. This inaccuracy stemmed from the algorithm's incorrect assumption of rectangular conductor geometries, whereas the true conductors are triangular.

In contrast, the inversion with correct localized discontinuities and $bv = 10^{-2}$ yielded a model with an ABIC of 1046.3 and a rms data misfit of 0.94 (Figure 12d). The significantly lower ABIC for the correct boundaries suggests that the development of a more advanced search method for finding the optimal boundaries based on ABIC minimization could enable the identification of the complex sharp boundaries, without prior information on the shape and locations of sharp boundaries.

Future directions for the SBI algorithm

Determining the correct positions and optimal weights for localized regularization adjustments remains challenging due to errors and limitations in prior information obtained from geophysical, geological, and drilling data (Hermans et al., 2012; Johnson et al., 2012; Zhou et al., 2014). In contrast, the SBI algorithm determines the correct positions and optimal weights for the

Downloaded 02/13/25 to 130.54.130.252. Redistribution subject to SEG license or copyright; see Terms of Use at http://library.seg.org/page/policies/terms
DOI:10.1190/geo2024-0365.1

This paper presented here as accepted for publication in Geophysics prior to copyediting and composition.
© 2025 The Authors. Published by the Society of Exploration Geophysicists.

Downloaded 02/13/25 to 130.54.130.252. Redistribution subject to SEG license or copyright; see Terms of Use at http://library.seg.org/page/policies/terms
DOI:10.1190/geo2024-0365.1

localized regularization adjustments by searching to minimize ABIC. Therefore, it facilitates the application of localized discontinuities in scenarios where prior information on sharp boundary locations is limited, unlike existing methods that determine the positions and weights of localized discontinuities based on prior information.

The SBI algorithm was applied to rectangular targets, assuming that the target shape was rectangular. However, target shapes can be more complex than rectangles, and prior information on their shape is often unavailable. One approach for recovering sharp boundaries of a complex structure without prior information is to combine sparse regularization inversions with the SBI algorithm. Sparse inversions require additional parameters that control the sharpness of the model structure and the inversions using different parameter values yield different sharp boundary representations of a target structure. The SBI algorithm may reproduce complex boundaries by using boundary representations obtained from the sparse inversions as initial values in the ABIC search. Moreover, modeling techniques using unstructured grids (Günther et al., 2006; Ren and Tang, 2010; Ishizu et al., 2019b; Jahandari et al., 2023) are effective in accurately representing complex structures. Future research directions include incorporating an advanced modeling technique into the SBI algorithm and recovering complex sharp boundaries.

Smoothing inversions of other geophysical data such as gravity, magnetic, and electromagnetic data also cannot recover sharp boundaries. We expect the SBI algorithm to be applicable to other geophysical data inversions to delineate sharp boundaries. Existing inversion codes can implement the SBI algorithm by simple modifications such as adding localized weight adjustments to the regularization and computation of ABIC. For example, Ishizu et al. (2022, 2024b) delineated deep-sea massive sulfides using smoothing inversions of controlled source electromagnetic data. However, the blurred boundaries could result in an incorrect evaluation of

This paper presented here as accepted for publication in Geophysics prior to copyediting and composition.
© 2025 The Authors. Published by the Society of Exploration Geophysicists.

their size. Controlled source electromagnetic inversions employing the SBI algorithm are anticipated to delineate sharp boundaries of massive sulfide deposits.

CONCLUSION

We developed an SBI algorithm using ABIC to delineate sharp resistivity boundaries of subsurface structures. The delineation of sharp boundaries is imperative for the precise evaluation of the location and attributes of sharp boundary structures. The developed SBI algorithm used localized regularization adjustments and determined the correct positions and optimal weights for these regularization adjustments by searching to minimize ABIC. A synthetic modeling study demonstrated that the SBI algorithm correctly delineated the sharp boundaries of a conductor. The ABIC was smallest when the positions of localized regularization adjustments were set correctly. In contrast, traditional smoothing inversion recovered the conductor with blurred outlines. The rms data misfits were 0.73 and 1.04 and final λ were 2.5 and 5011.8 for the smooth model and the model obtained by the developed algorithm, respectively. This indicates that ABIC with correctly placed localized discontinuities achieved through regularization adjustment prioritized the regularization term over the data misfit term. The application to field data demonstrated that the SBI algorithm with the smallest ABIC delineated the sharp boundaries of a utility tunnel. The size and horizontal position of the recovered tunnel were consistent with the estimated size and horizontal position based on the blueprint. The synthetic and field data studies prove that the developed SBI algorithm effectively delineates sharp boundaries that are difficult to recover using traditional smoothing inversion algorithms.

Downloaded 02/13/25 to 130.54.130.252. Redistribution subject to SEG license or copyright; see Terms of Use at http://library.seg.org/page/policies/terms
DOI:10.1190/geo2024-0365.1

© 2025 The Authors. Published by the Society of Exploration Geophysicists.

The SBI algorithm can be used for various geophysical survey data, as it is applicable even when prior information on sharp boundary locations is limited, unlike existing methods that determine the positions and weights of localized regularization adjustments based on prior information. Future research directions include incorporating additional modeling techniques, such as finite element modeling, into the SBI algorithm and applying these additional modeling techniques to delineate more complex sharp boundaries.

ACKNOWLEDGMENTS

We are grateful to three anonymous reviewers, editors Antoine Guitton, Sihong Wu, and Colin Farquharson for their insightful feedback, which has significantly enhanced this work. We also thank the facilities management department of Kyoto University for their assistance in providing information on the utility tunnel. This work was supported by the Japan Society for the Promotion of Science KAKENHI (grants 17J08764 and 22K14104)

REFERENCES

Akaike, H., 1980, Likelihood and the Bayes procedure, in Bayesian statistics, Vol. 31. University Press, 143–166.

Amatyakul, P., C. Vachiratienchai, and W. Siripunvaraporn, 2017, WSJointInv2D-MT-DCR: An efficient joint two-dimensional magnetotelluric and direct current resistivity inversion: Computers & Geosciences, 102, 100–108.

André, F., C. van Leeuwen, S. Saussez, R. Van Durmen, P. Bogaert, D. Moghadas, L. de Rességuier, B. Delvaux, H. Vereecken, and S. Lambot, 2012, High-resolution imaging of a

Downloaded 02/13/25 to 130.54.130.252. Redistribution subject to SEG license or copyright; see Terms of Use at http://library.seg.org/page/policies/terms
DOI:10.1190/geo2024-0365.1

This paper presented here as accepted for publication in Geophysics prior to copyediting and composition.
© 2025 The Authors. Published by the Society of Exploration Geophysicists.

vineyard in south of France using ground-penetrating radar, electromagnetic induction and electrical resistivity tomography: Journal of Applied Geophysics, 78, 113–122.

Asaue, H., K. Koike, T. Yoshinaga, T. Goto, and H. Yoshida, 2021, Development and Application of a Variable-Frequency-Based Electric Sounding System for Increasing the Accuracy of Aquifer Detection: Natural Resources Research, 30, 3017–3034.

Binley, A., and L. Slater, 2020, Resistivity and Induced Polarization: Theory and Applications to the Near-Surface Earth: Cambridge University Press.

Chambers, J. E., O. Kuras, P. I. Meldrum, R. D. Ogilvy, and J. Hollands, 2006, Electrical resistivity tomography applied to geologic, hydrogeologic, and engineering investigations at a former waste-disposal site: Geophysics, 71, B231–B239.

Constable, S. C., R. L. Parker, and C. G. Constable, 1987, Occam's inversion: A practical algorithm for generating smooth models from electromagnetic sounding data: Geophysics, 52, 289–300.

Dahlin, T., and M. Loke, 2018, Underwater ERT surveying in water with resistivity layering with example of application to site investigation for a rock tunnel in central Stockholm: Near Surface Geophysics, 16, 230–237.

Deleersnyder, W., B. Maveau, T. Hermans, and D. Dudal, 2023, Flexible quasi-2D inversion of time-domain AEM data, using a wavelet-based complexity measure: Geophysical Journal International, **233**, 1847–1862.

Doetsch, J., N. Linde, M. Pessognelli, A. G. Green, and T. Günther, 2012, Constraining 3-D electrical resistance tomography with GPR reflection data for improved aquifer characterization: Journal of Applied Geophysics, 78, 68–76.

Downloaded 02/13/25 to 130.54.130.252. Redistribution subject to SEG license or copyright; see Terms of Use at http://library.seg.org/page/policies/terms
DOI:10.1190/geo2024-0365.1

This paper presented here as accepted for publication in Geophysics prior to copyediting and composition.
© 2025 The Authors. Published by the Society of Exploration Geophysicists.

Farquharson, C. G., 2008, Constructing piecewise-constant models in multidimensional minimum-structure inversions: Geophysics, **73**, K1–K9.

Fukahata, Y., 2012, Inversion Analyses Based on ABIC with Non-full Rank Prior Information: Zisin, 64, 91–95.

Fukahata, Y., and M. Hashimoto, 2016, Simultaneous estimation of the dip angles and slip distribution on the faults of the 2016 Kumamoto earthquake through a weak nonlinear inversion of InSAR data: Earth, Planets and Space, 68, 204.

Fukahata, Y., A. Nishitani, and M. Matsu'ura, 2004, Geodetic data inversion using ABIC to estimate slip history during one earthquake cycle with viscoelastic slip-response functions: Geophysical Journal International, 156, 140–153.

Goto, T., T. Kasaya, H. Machiyama, R. Takagi, R. Matsumoto, Y. Okuda, M. Satoh, T. Watanabe, N. Seama, H. Mikada, Y. Sanada, and M. Kinoshita, 2008, A marine deep-towed DC resistivity survey in a methane hydrate area, Japan Sea: Exploration Geophysics, 39, 52–59.

Gresse, M., J. Vandemeulebrouck, S. Byrdina, G. Chiodini, A. Revil, T. C. Johnson, T. Ricci, G. Vilardo, A. Mangiacapra, T. Lebourg, J. Grangeon, P. Bascou, and L. Metral, 2017, Three-Dimensional Electrical Resistivity Tomography of the Solfatara Crater (Italy): Implication for the Multiphase Flow Structure of the Shallow Hydrothermal System: Journal of Geophysical Research: Solid Earth, 122, 8749–8768.

Günther, T., C. Rücker, and K. Spitzer, 2006, Three-dimensional modelling and inversion of dc resistivity data incorporating topography — II. Inversion: Geophysical Journal International, 166, 506–517.

Downloaded 02/13/25 to 130.54.130.252. Redistribution subject to SEG license or copyright; see Terms of Use at http://library.seg.org/page/policies/terms
DOI:10.1190/geo2024-0365.1

This paper presented here as accepted for publication in Geophysics prior to copyediting and composition.
© 2025 The Authors. Published by the Society of Exploration Geophysicists.

Hermans, T., A. Vandenbohede, L. Lebbe, R. Martin, A. Kemna, J. Beaujean, and F. Nguyen, 2012, Imaging artificial salt water infiltration using electrical resistivity tomography constrained by geostatistical data: Journal of Hydrology, 438–439, 168–180.

Hung, Y.-C., Y.-X. Zhao, and W.-C. Hung, 2022, Development of an Underground Tunnels Detection Algorithm for Electrical Resistivity Tomography Based on Deep Learning: Applied Sciences, 12.

Ishizu, K., C. Vachiratienchai, W. Siripunvaraporn, T. Goto, T. Kasaya, and H. Iwamoto, 2019a, Evaluations of effectiveness of marine deep-towed DC resistivity survey in investigation of seafloor massive sulfide deposits: BUTSURI-TANSA(Geophysical Exploration), 72, 122–138.

Ishizu, K., W. Siripunvaraporn, T. Goto, K. Koike, T. Kasaya, and H. Iwamoto, 2022, A cost-effective three-dimensional marine controlled-source electromagnetic survey: Exploring seafloor massive sulfides: Geophysics, 87, E219–E241.

Ishizu, K., A. Oda, T. Goto, T. Kasaya, T. Watanabe, and H. Machiyama, 2024a, Electrical resistivity tomography combined with seismic data estimates heterogeneous distribution of near-seafloor concentrated gas hydrates within gas chimneys: Scientific Reports, 14, 15045.

Ishizu, K., T. Kasaya, T.-N. Goto, K. Koike, W. Siripunvaraporn, H. Iwamoto, Y. Kawada, and J.-I. Ishibashi, 2024b, A marine controlled-source electromagnetic application using towed and seafloor-based receivers capable of mapping seafloor and embedded massive sulfides: Geophysics, 89, E87–E99.

Ishizu, K., T. Goto, Y. Ohta, T. Kasaya, H. Iwamoto, C. Vachiratienchai, W. Siripunvaraporn, T. Tsuji, H. Kumagai, and K. Koike, 2019b, Internal Structure of a Seafloor Massive Sulfide

Downloaded 02/13/25 to 130.54.130.252. Redistribution subject to SEG license or copyright; see Terms of Use at http://library.seg.org/page/policies/terms
DOI:10.1190/geo2024-0365.1

This paper presented here as accepted for publication in Geophysics prior to copyediting and composition.
© 2025 The Authors. Published by the Society of Exploration Geophysicists.

Deposit by Electrical Resistivity Tomography, Okinawa Trough: Geophysical Research Letters, 46, 11025–11034.

Jahandari, H., P. Lelièvre, and C. G. Farquharson, 2023, Forward modeling of direct-current resistivity data on unstructured grids using an adaptive mimetic finite-difference method: Geophysics, 88, E123–E134.

Johnson, T. C., R. J. Versteeg, M. Rockhold, L. D. Slater, D. Ntarlagiannis, W. J. Greenwood, and J. Zachara, 2012, Characterization of a contaminated wellfield using 3D electrical resistivity tomography implemented with geostatistical, discontinuous boundary, and known conductivity constraints: Geophysics, 77, EN85–EN96.

Kemna, A., J. Vanderborght, B. Kulessa, and H. Vereecken, 2002, Imaging and characterisation of subsurface solute transport using electrical resistivity tomography (ERT) and equivalent transport models: Journal of Hydrology, 267, 125–146.

Key, K., 2009, 1D inversion of multicomponent, multifrequency marine CSEM data: Methodology and synthetic studies for resolving thin resistive layers: Geophysics, 74, F9–F20.

Kimura, T., T. Goto, T. Kasaya, T. Okamoto, H. Mikada, Y. Sanada, T. Watanabe, and Y. Ashida, 2010, Two-dimensional inversion of magnetotelluric data with sharp structural boundary: BUTSURI-TANSA(Geophysical Exploration), 63, 185–196.

Klose, T., J. Guillemoteau, G. Vignoli, and J. Tronicke, 2022, Laterally constrained inversion (LCI) of multi-configuration EMI data with tunable sharpness: Journal of Applied Geophysics, **196**, 104519.

Downloaded 02/13/25 to 130.54.130.252. Redistribution subject to SEG license or copyright; see Terms of Use at http://library.seg.org/page/policies/terms
DOI:10.1190/geo2024-0365.1

This paper presented here as accepted for publication in Geophysics prior to copyediting and composition.
© 2025 The Authors. Published by the Society of Exploration Geophysicists.

Kyoto Prefecture Office, 2005, Report on active fault survey in Kyoto Prefecture (Kyoto University Katsura campus area), 33 pp. Retrieved from https://www.pref.kyoto.jp/kikikanri/documents/kazi_rep.pdf (accessed on August 17, 2024).

Lapenna, V., P. Lorenzo, A. Perrone, S. Piscitelli, E. Rizzo, and F. Sdao, 2005, 2D electrical resistivity imaging of some complex landslides in Lucanian Apennine chain, southern Italy: Geophysics, 70, B11–B18.

Loke, M. H., I. Acworth, and T. Dahlin, 2003, A comparison of smooth and blocky inversion methods in 2D electrical imaging surveys: Exploration Geophysics, 34, 182–187.

Misonou, T., H. Asaue, T. Yoshinaga, Y. Matsukuma, K. Koike, and J. Shimada, 2013, Hydrogeologic-structure and groundwater-movement imaging in tideland using electrical sounding resistivity: a case study on the Ariake Sea coast, southwest Japan: Hydrogeology Journal, 21, 1593–1603.

Mitsuhata, Y., T. Uchida, and H. Amano, 2002, 2.5-D inversion of frequency-domain electromagnetic data generated by a grounded-wire source: Geophysics, 67, 1753–1768.

Ogawa, Y., and T. Uchida, 1996, A two-dimensional magnetotelluric inversion assuming Gaussian static shift: Geophysical Journal International, 126, 69–76.

Ren, Z., and J. Tang, 2010, 3D direct current resistivity modeling with unstructured mesh by adaptive finite-element method: Geophysics, 75, H7–H17.

Revil, A., T. C. Johnson, and A. Finizola, 2010, Three-dimensional resistivity tomography of Vulcan's forge, Vulcano Island, southern Italy: Geophysical Research Letters, 37, L15308.

Rizzo, E., A. Colella, V. Lapenna, and S. Piscitelli, 2004, High-resolution images of the fault-controlled High Agri Valley basin (Southern Italy) with deep and shallow electrical resistivity tomographies: Physics and Chemistry of the Earth, Parts A/B/C, 29, 321–327.

Downloaded 02/13/25 to 130.54.130.252. Redistribution subject to SEG license or copyright; see Terms of Use at http://library.seg.org/page/policies/terms.
DOI:10.1190/geo2024-0365.1

This paper presented here as accepted for publication in Geophysics prior to copyediting and composition.
© 2025 The Authors. Published by the Society of Exploration Geophysicists.

Sasaki, Y., 1994, 3-D resistivity inversion using the finite-element method: Geophysics, 59, 1839–1848.

Satitpittakul, A., C. Vachiratienchai, and W. Siripunvaraporn, 2013, Factors influencing cavity detection in Karst terrain on two-dimensional (2-D) direct current (DC) resistivity survey: A case study from the western part of Thailand: Engineering Geology, 152, 162–171.

Slater, L., and A. Binley, 2006, Synthetic and field-based electrical imaging of a zerovalent iron barrier: Implications for monitoring long-term barrier performance: Geophysics, 71, B129–B137.

Soueid Ahmed, A., A. Revil, S. Byrdina, A. Coperey, L. Gailler, N. Grobbe, F. Viveiros, C. Silva, D. Jougnot, A. Ghorbani, C. Hogg, D. Kiyan, V. Rath, M. J. Heap, H. Grandis, and H. Humaida, 2018, 3D electrical conductivity tomography of volcanoes: Journal of Volcanology and Geothermal Research, 356, 243–263.

Uchida, T., 1993a, Smoothness-constraint 2D inversion for DC resistivity data by ABIC minimization method: Butsuri-Tansa, 46, 105–119.

Uchida, T., 1993b, Smooth 2-D Inversion for Magnetotelluric Data Based on Statistical Criterion ABIC: Journal of Geomagnetism and Geoelectricity, 45, 841–858.

Vachiratienchai, C., and W. Siripunvaraporn, 2013, An efficient inversion for two-dimensional direct current resistivity surveys based on the hybrid finite difference–finite element method: Physics of the Earth and Planetary Interiors, 215, 1–11.

Vignoli, G., G. Fiandaca, A. V. Christiansen, C. Kirkegaard, and E. Auken, 2015, Sharp spatially constrained inversion with applications to transient electromagnetic data: Geophysical Prospecting, **63**, 243–255.

Downloaded 02/13/25 to 130.54.130.252. Redistribution subject to SEG license or copyright; see Terms of Use at http://library.seg.org/page/policies/terms
DOI:10.1190/geo2024-0365.1

This paper presented here as accepted for publication in Geophysics prior to copyediting and composition.
© 2025 The Authors. Published by the Society of Exploration Geophysicists.

Wang, S., T. Kalscheuer, M. Bastani, A. Malehmir, L. B. Pedersen, T. Dahlin, and N. Meqbel, 2018, Joint inversion of lake-floor electrical resistivity tomography and boat-towed radio-magnetotelluric data illustrated on synthetic data and an application from the Äspö Hard Rock Laboratory site, Sweden: Geophysical Journal International, 213, 511–533.

Yabuki, T., and M. Matsu'ura, 1992, Geodetic data inversion using a Bayesian information criterion for spatial distribution of fault slip: Geophysical Journal International, 109, 363–375.

Zhou, J., A. Revil, M. Karaoulis, D. Hale, J. Doetsch, and S. Cuttler, 2014, Image-guided inversion of electrical resistivity data: Geophysical Journal International, 197, 292–309.

LIST OF FIGURES

Figure 1. Schematic diagram of the developed SBI algorithm using ABIC minimization to determine correct positions and optimal weights for localized regularization adjustments to delineate sharp boundaries.

Figure 2. Test model for generating synthetic datasets. A 10-Ωm conductor with sharp boundaries is embedded in a 100-Ωm homogeneous half-space structure. The conductor shape is a rectangle of 20–26 m and 1.5–6 m for the *x*- and *z*-directions, respectively. Magenta lines represent the outlines of the conductor. The vertical exaggeration is 2.

Figure 3. Smooth model and its roughness. (a) Inverted model of synthetic data obtained using smoothness regularization. Magenta lines represent the true outline of the conductor ($x = 20$ m and $x = 26$ m; $z = 1.5$ m and $z = 6$ m). (b) and (c) show the absolute of the roughness of the smooth model in (a) for the *x*- and *z*-directions, respectively. Red lines indicate our initial sharp boundary location ($x = 19$ m and $x = 27$ m; $z = 1$ m and $z = 7$ m).

Downloaded 02/13/25 to 130.54.130.252. Redistribution subject to SEG license or copyright; see Terms of Use at http://library.seg.org/page/policies/terms
DOI:10.1190/geo2024-0365.1

This paper presented here as accepted for publication in Geophysics prior to copyediting and composition.
© 2025 The Authors. Published by the Society of Exploration Geophysicists.

Figure 4. Inverted models of synthetic data obtained from the SBI algorithm. (a) Inverted model with localized regularization adjustments for x = 19 m and x = 27 m; z = 1 m and z = 7 m (initial location). (b) Inverted model with localized regularization adjustments for x = 20 m and x = 26 m; z = 1 m and z = 7 m (Flow 3). (c) Inverted model with localized regularization adjustments for x = 20 m and x = 26 m; z = 1.5 m and z = 6 m (Flow 4; optimal model). Magenta lines represent the true outline of the conductor. The weight $bv = 10^{-2}$ is assigned for (a) and (b); $bv = 10^{-3}$ is assigned for (c).

Figure 5. Cross-plots of ABIC as a function of the left boundary discontinuity location for regularization adjustments, (a) λ, (b) rms misfit, and (c) bv. Localized regularization adjustments are also applied for true positions for right, top, and bottom boundaries.

Figure 6. Plots of the ABIC and rms misfit as functions of the left boundary discontinuity location for regularization adjustments, λ, and bv. (a) Smoothness inversion result, and (b), (c), and (d) SBI results with left boundary positions of 18 m, 19 m, and 20 m, respectively. Within each panel of (b)–(d), the left, center, and right plots correspond to bv values of 10^{-1}, 10^{-2}, and 10^{-3}, respectively. Localized regularization adjustments are also implemented for the true positions of the right, top, and bottom boundaries. The black dot indicates the minimum ABIC point, while the black dashed line represents the λ value associated with the minimum ABIC. The black solid line indicates the λ value associated with the minimum rms misfit.

Figure 7. Inverted models of synthetic data obtained from the SBI algorithm using vertical grids not aligned with a true top position of z = 1.5 m. (a) Inverted model with localized regularization adjustments for z = 1.2 m (nearest top vertical grid of z = 1.2 m). (b) Inverted model with localized regularization adjustments for z = 1.8 m (nearest top vertical grid of z =

Downloaded 02/13/25 to 130.54.130.252. Redistribution subject to SEG license or copyright; see Terms of Use at http://library.seg.org/page/policies/terms
DOI:10.1190/geo2024-0365.1

This paper presented here as accepted for publication in Geophysics prior to copyediting and composition.
© 2025 The Authors. Published by the Society of Exploration Geophysicists.

1.8 m). (c) Relationship between ABIC and nearest grid position. Localized regularization adjustments are also applied for x = 20 m, x = 26 m, and z = 6 m.

Figure 8. Location of an ERT survey along a promenade on a campus of Kyoto University. The survey target is a utility tunnel with sharp rectangular boundaries. A blueprint indicates its horizontal width and vertical thickness as 3.5 m and 4.4 m, respectively. Dashed black lines indicate its horizontal location estimated from the blueprint, and the center is 14 m. The thick black line indicates the 54 m survey profile.

Figure 9. Observed ERT data, smooth model of the field data, and its first-derivative roughness. (a) Observed apparent resistivity data. The vertical axis represents pseudo depth in units of nLevel, where nLevel is the distance between the source and receiver electrodes divided by our basic electrode spacing of 2 m. (b) Inverted model using smoothness regularization. Black lines with a double arrow indicate the horizontal location of the tunnel (x = 12.25–15.75 m) determined based on the blueprint and the center is 14 m. (c) and (d) show the absolute of the first-derivative roughness of the inverted model in (b) for the x- and z-directions, respectively. Red lines indicate our initial sharp boundary location (x = 11 m and x =17 m; z = 1.5 m and z = 7 m).

Figure 10. Inversion results of the field data obtained from the SBI algorithm. (a) Inverted model with localized regularization adjustments for an initial location of x = 11 m and x = 17 m; z = 1.5 m and z = 7 m. (b) Inverted model with localized regularization adjustments for x = 12 m and x = 16 m; z = 1.5 m and z = 7 m after Flow 3. (c) Inverted model with localized regularization adjustments for x = 12 m and x = 16 m; z = 2 m and z = 7 m after Flow 4. $bv = 10^{-1}$ is assigned for obtaining the models shown in Figure 9a–c. Black lines with double

Downloaded 02/13/25 to 130.54.130.252. Redistribution subject to SEG license or copyright; see Terms of Use at http://library.seg.org/page/policies/terms
DOI:10.1190/geo2024-0365.1

This paper presented here as accepted for publication in Geophysics prior to copyediting and composition.
© 2025 The Authors. Published by the Society of Exploration Geophysicists.

arrows indicate the horizontal location of the tunnel (x = 12.25–15.75 m) determined based on the blueprint, and the center is 14 m.

Figure 11. True model including the triangular structures, smooth inversion result, and its first-derivative roughness. (a) Two 10 Ωm triangular structures with upward and downward orientations (A1 and A2), are embedded in a 100 Ωm homogeneous half-space structure. (b) Inverted model using smoothness regularization. Magenta lines represent the true outline of the conductors. (c) and (d) present the absolute of the first-derivative roughness of the inverted model in (b) for the x- and z-directions, respectively. Light blue lines indicate our initial sharp boundary locations (A1: x = 13 m and x =16 m; z = 1.5 m and z = 7 m, and A2: x = 30 m and x =39 m; z = 1 m and z = 4 m).

Figure 12. Inversion results of the synthetic data generated from the model, including the triangular structures (Figure 11a). Inverted models obtained by the SBI algorithm for (a) A1, (b) A2, and (c) both A1 and A2. (d) Inverted model with localized regularization adjustments for true sharp boundaries. The parameter bv was set to 10^{-1} to obtain the models depicted in Figure 11a and 11b, and to 10^{-2} in Figure 11c and 11d.

Figure A1. Inverted models obtained with bv ranging from 10^{-4} to 1 and localized regularization adjustments for x = 20 m and x = 26 m; z = 1.5 m and z = 6 m. bv = (a) 1, (b) 10^{-1}, (c) 10^{-2}, (d) 10^{-3}, and (e) 10^{-4}. Magenta lines represent the true outline of the conductor. (a) and (d) are the same for Figures 3a and 4c.

Downloaded 02/13/25 to 130.54.130.252. Redistribution subject to SEG license or copyright; see Terms of Use at http://library.seg.org/page/policies/terms
DOI:10.1190/geo2024-0365.1

This paper presented here as accepted for publication in Geophysics prior to copyediting and composition.
© 2025 The Authors. Published by the Society of Exploration Geophysicists.

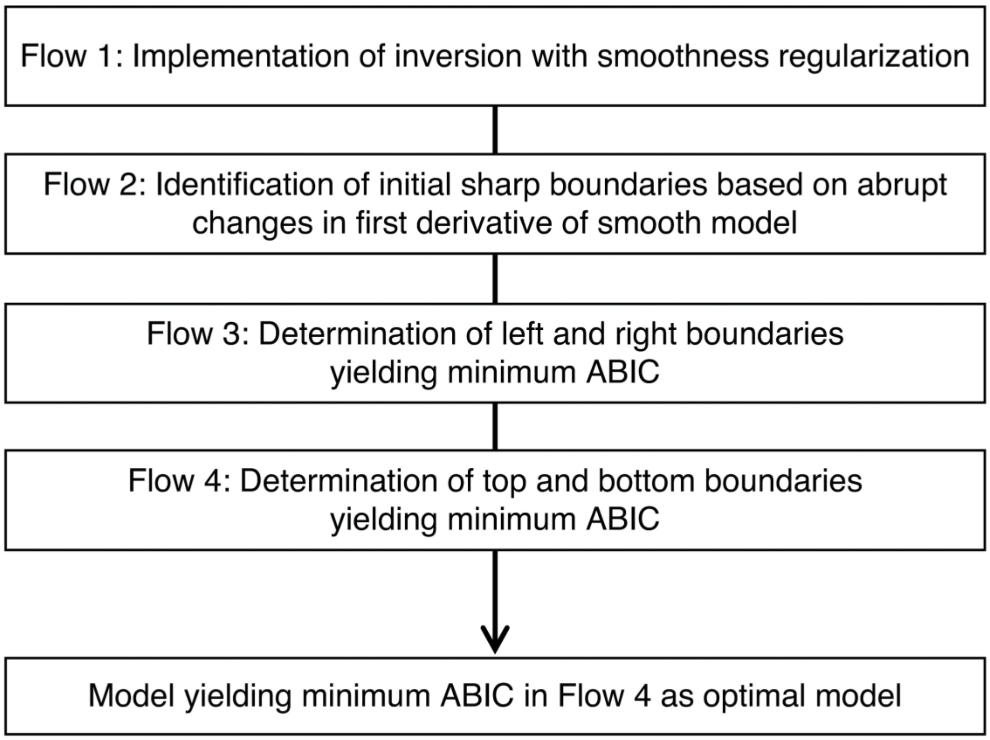

Figure 1. Schematic diagram of the developed SBI algorithm using ABIC minimization to determine correct positions and optimal weights for localized regularization adjustments to delineate sharp boundaries.

220x161mm (300 x 300 DPI)

Downloaded 02/13/25 to 130.54.130.252. Redistribution subject to SEG license or copyright; see Terms of Use at http://library.seg.org/page/policies/terms
DOI:10.1190/geo2024-0365.1

This paper presented here as accepted for publication in Geophysics prior to copyediting and composition.
© 2025 The Authors. Published by the Society of Exploration Geophysicists.

Downloaded 02/13/25 to 130.54.130.252. Redistribution subject to SEG license or copyright; see Terms of Use at http://library.seg.org/page/policies/terms
DOI:10.1190/geo2024-0365.1

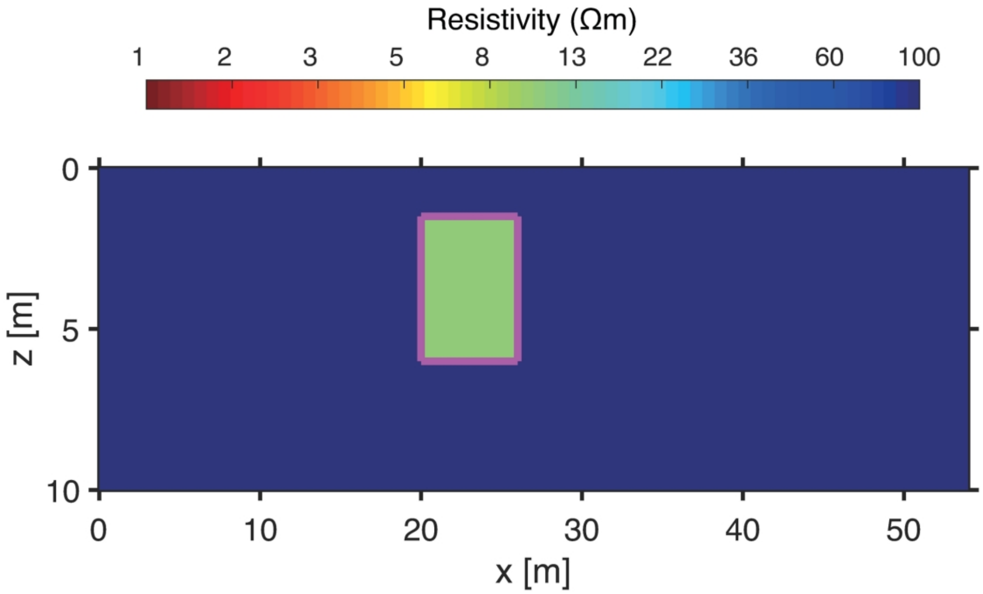

Figure 2. Test model for generating synthetic datasets. A 10-Ωm conductor with sharp boundaries is embedded in a 100-Ωm homogeneous half-space structure. The conductor shape is a rectangle of 20–26 m and 1.5–6 m for the x- and z-directions, respectively. Magenta lines represent the outlines of the conductor. The vertical exaggeration is 2.

188x113mm (300 x 300 DPI)

This paper presented here as accepted for publication in Geophysics prior to copyediting and composition.
© 2025 The Authors. Published by the Society of Exploration Geophysicists.

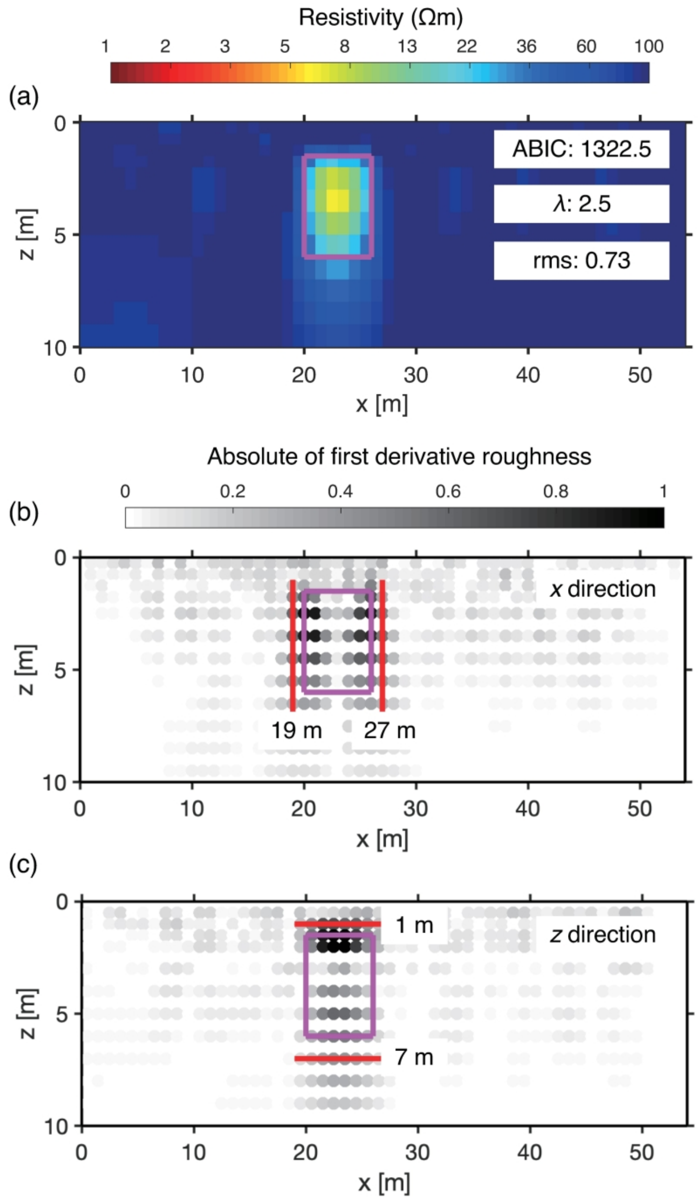

Figure 3. Smooth model and its roughness. (a) Inverted model of synthetic data obtained using smoothness regularization. Magenta lines represent the true outline of the conductor (x = 20 m and x = 26 m; z = 1.5 m and z = 6 m). (b) and (c) show the absolute of the roughness of the smooth model in (a) for the x- and z-directions, respectively. Red lines indicate our initial sharp boundary location (x = 19 m and x = 27 m; z = 1 m and z = 7 m).

212x324mm (300 x 300 DPI)

Downloaded 02/13/25 to 130.54.130.252. Redistribution subject to SEG license or copyright; see Terms of Use at http://library.seg.org/page/policies/terms.
DOI:10.1190/geo2024-0365.1

This paper presented here as accepted for publication in Geophysics prior to copyediting and composition.
© 2025 The Authors. Published by the Society of Exploration Geophysicists.

Downloaded 02/13/25 to 130.54.130.252. Redistribution subject to SEG license or copyright; see Terms of Use at http://library.seg.org/page/policies/terms
DOI:10.1190/geo2024-0365.1

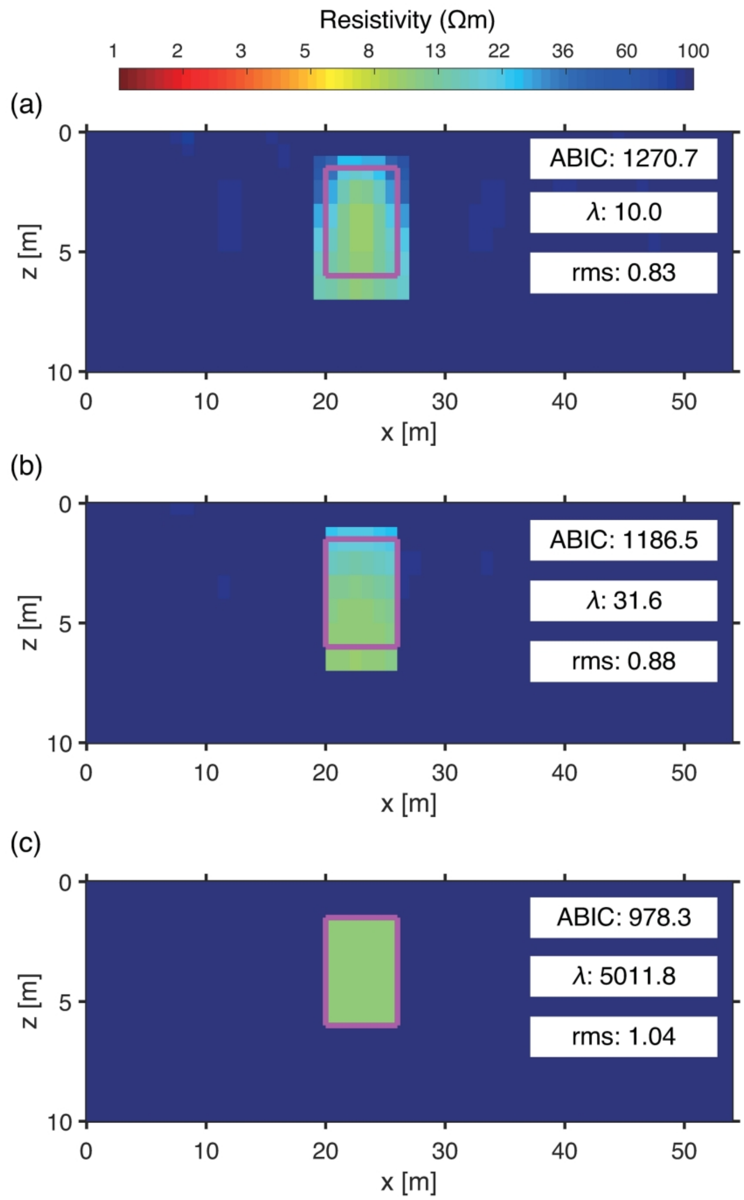

Figure 4. Inverted models of synthetic data obtained from the SBI algorithm. (a) Inverted model with localized regularization adjustments for x = 19 m and x = 27 m; z = 1 m and z = 7 m (initial location). (b) Inverted model with localized regularization adjustments for x = 20 m and x = 26 m; z = 1 m and z = 7 m (Flow 3). (c) Inverted model with localized regularization adjustments for x = 20 m and x = 26 m; z = 1.5 m and z = 6 m (Flow 4; optimal model). Magenta lines represent the true outline of the conductor. The weight bv = 10−2 is assigned for (a) and (b); bv = 10−3 is assigned for (c).

211x304mm (300 x 300 DPI)

This paper presented here as accepted for publication in Geophysics prior to copyediting and composition.
© 2025 The Authors. Published by the Society of Exploration Geophysicists.

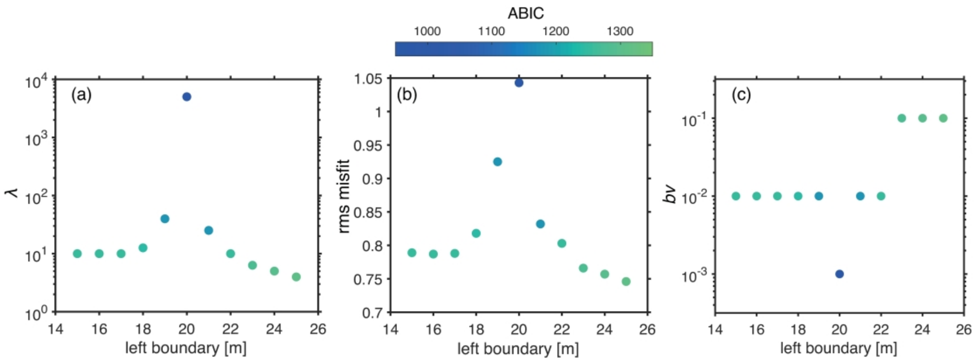

Figure 5. Cross-plots of ABIC as a function of the left boundary discontinuity location for regularization adjustments, (a) λ, (b) rms misfit, and (c) bv. Localized regularization adjustments are also applied for true positions for right, top, and bottom boundaries.

403x145mm (300 x 300 DPI)

Downloaded 02/13/25 to 130.54.130.252. Redistribution subject to SEG license or copyright; see Terms of Use at http://library.seg.org/page/policies/terms
DOI:10.1190/geo2024-0365.1

© 2025 The Authors. Published by the Society of Exploration Geophysicists.

Downloaded 02/13/25 to 130.54.130.252. Redistribution subject to SEG license or copyright; see Terms of Use at http://library.seg.org/page/policies/terms
DOI:10.1190/geo2024-0305.1

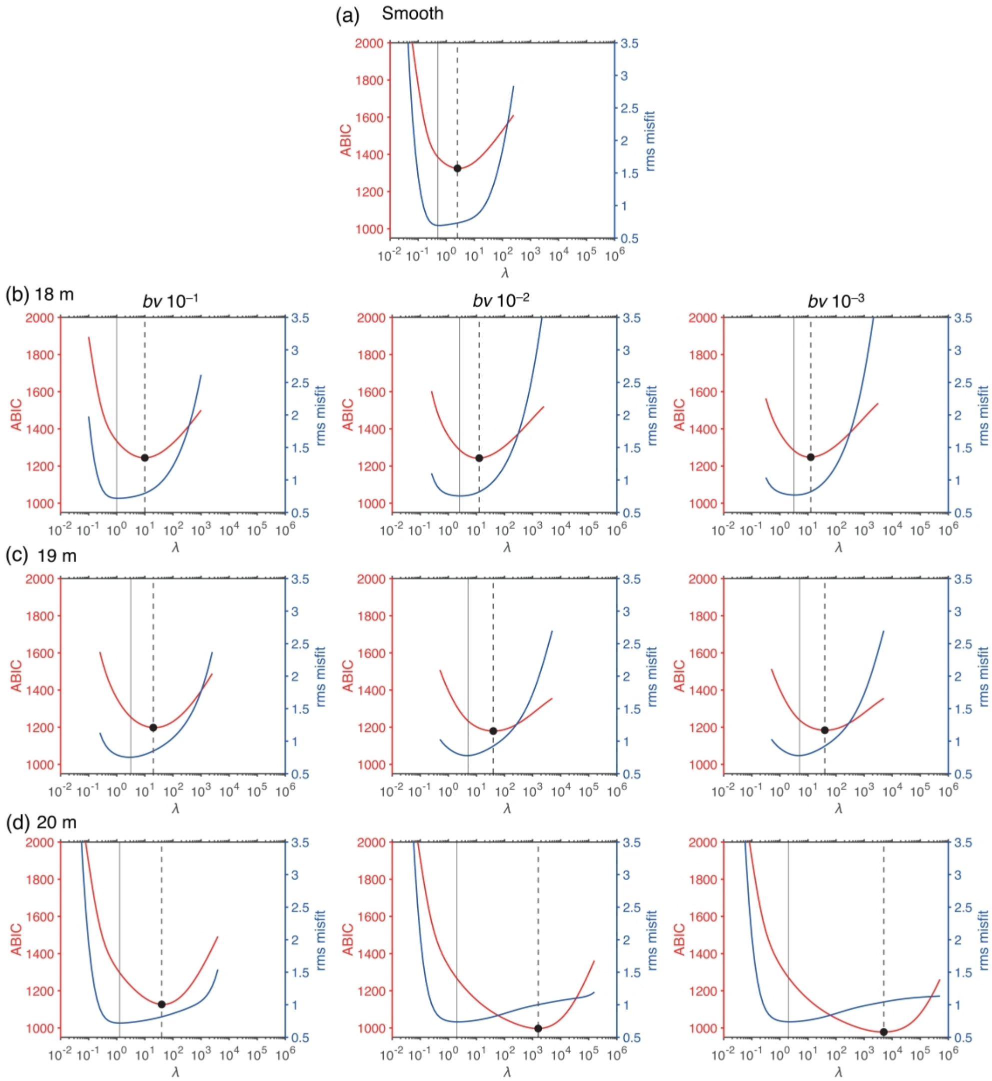

Figure 6. Plots of the ABIC and rms misfit as functions of the left boundary discontinuity location for regularization adjustments, λ, and bv. (a) Smoothness inversion result, and (b), (c), and (d) SBI results with left boundary positions of 18 m, 19 m, and 20 m, respectively. Within each panel of (b)–(d), the left, center, and right plots correspond to bv values of 10−1, 10−2, and 10−3, respectively. Localized regularization adjustments are also implemented for the true positions of the right, top, and bottom boundaries. The black dot indicates the minimum ABIC point, while the black dashed line represents the λ value associated with the minimum ABIC. The black solid line indicates the λ value associated with the minimum rms misfit.

547x594mm (600 x 600 DPI)

This paper presented here as accepted for publication in Geophysics prior to copyediting and composition.
© 2025 The Authors. Published by the Society of Exploration Geophysicists.

Downloaded 02/13/25 to 130.54.130.252. Redistribution subject to SEG license or copyright; see Terms of Use at http://library.seg.org/page/policies/terms
DOI:10.1190/geo2024-0355.1

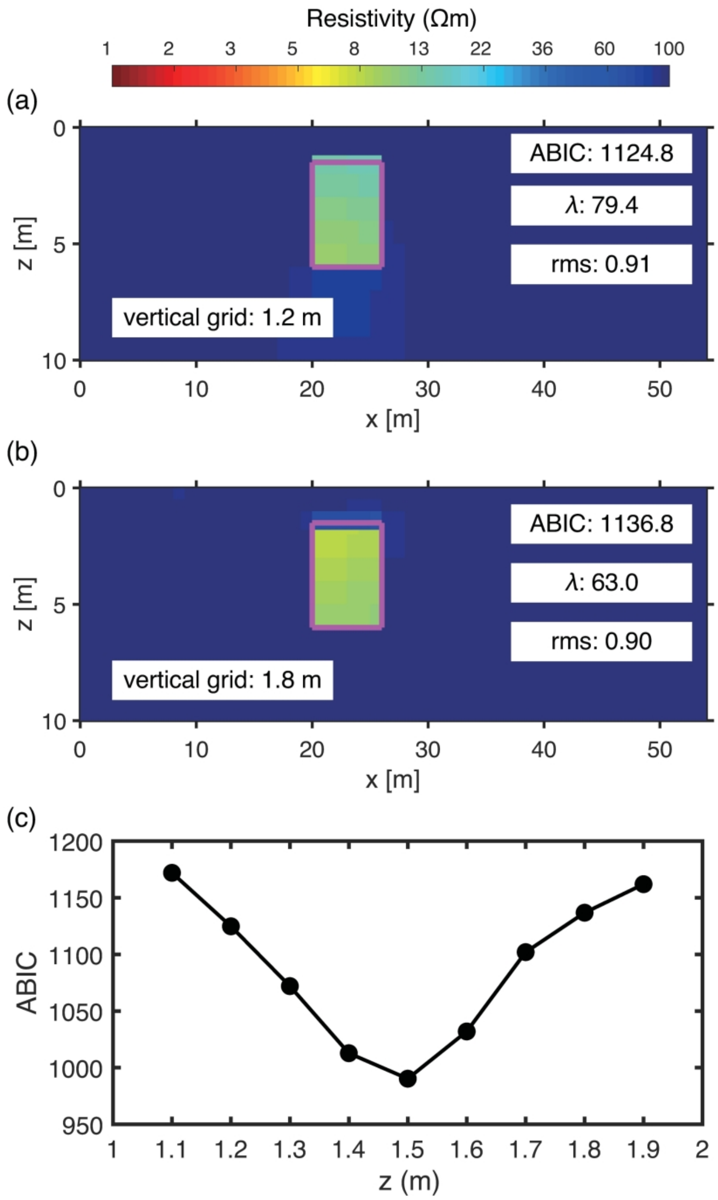

Figure 7. Inverted models of synthetic data obtained from the SBI algorithm using vertical grids not aligned with a true top position of z = 1.5 m. (a) Inverted model with localized regularization adjustments for z = 1.2 m (nearest top vertical grid of z = 1.2 m). (b) Inverted model with localized regularization adjustments for z = 1.8 m (nearest top vertical grid of z = 1.8 m). (c) Relationship between ABIC and nearest grid position. Localized regularization adjustments are also applied for x = 20 m, x = 26 m, and z = 6 m.

211x312mm (300 x 300 DPI)

This paper presented here as accepted for publication in Geophysics prior to copyediting and composition.
© 2025 The Authors. Published by the Society of Exploration Geophysicists.

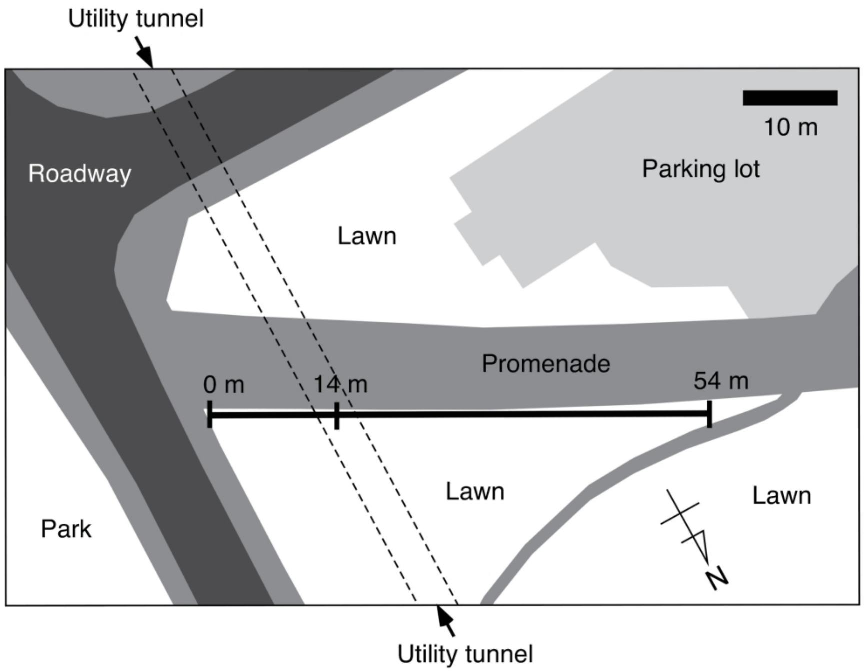

Figure 8. Location of an ERT survey along a promenade on a campus of Kyoto University. The survey target is a utility tunnel with sharp rectangular boundaries. A blueprint indicates its horizontal width and vertical thickness as 3.5 m and 4.4 m, respectively. Dashed black lines indicate its horizontal location estimated from the blueprint, and the center is 14 m. The thick black line indicates the 54 m survey profile.

224x177mm (300 x 300 DPI)

Downloaded 02/13/25 to 130.54.130.252. Redistribution subject to SEG license or copyright; see Terms of Use at http://library.seg.org/page/policies/terms
DOI:10.1190/geo2024-0365.1

This paper presented here as accepted for publication in Geophysics prior to copyediting and composition.
© 2025 The Authors. Published by the Society of Exploration Geophysicists.

Downloaded 02/13/25 to 130.54.130.252. Redistribution subject to SEG license or copyright; see Terms of Use at http://library.seg.org/page/policies/terms
DOI:10.1190/geo2024-0305.1

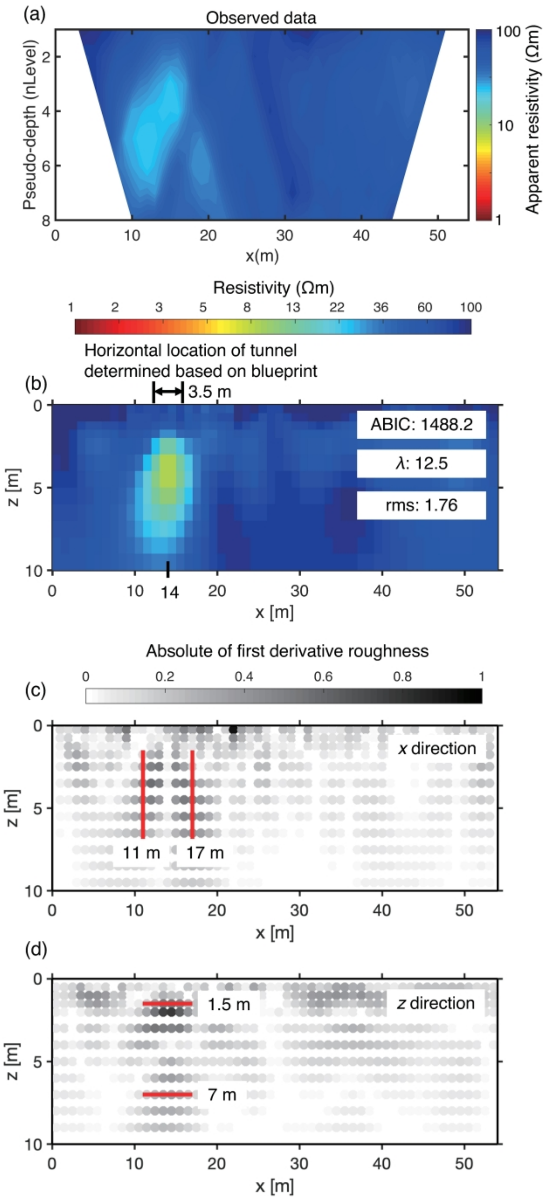

Figure 9. Observed ERT data, smooth model of the field data, and its first-derivative roughness. (a) Observed apparent resistivity data. The vertical axis represents pseudo depth in units of nLevel, where nLevel is the distance between the source and receiver electrodes divided by our basic electrode spacing of 2 m. (b) Inverted model using smoothness regularization. Black lines with a double arrow indicate the horizontal location of the tunnel (x = 12.25–15.75 m) determined based on the blueprint and the center is 14 m. (c) and (d) show the absolute of the first-derivative roughness of the inverted model in (b) for the x- and z-directions, respectively. Red lines indicate our initial sharp boundary location (x = 11 m and x =17 m; z = 1.5 m and z = 7 m).

212x440mm (300 x 300 DPI)

This paper presented here as accepted for publication in Geophysics prior to copyediting and composition.
© 2025 The Authors. Published by the Society of Exploration Geophysicists.

Downloaded 02/13/25 to 130.54.130.252. Redistribution subject to SEG license or copyright; see Terms of Use at http://library.seg.org/page/policies/terms
DOI:10.1190/geo2024-0395.1

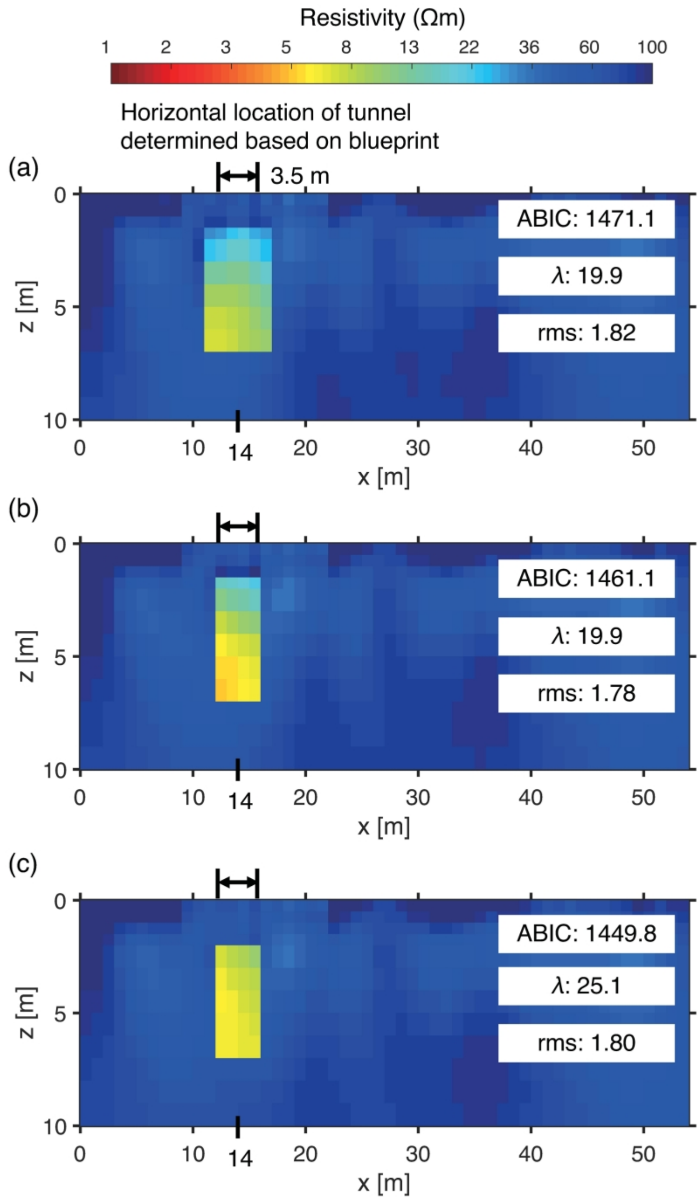

Figure 10. Inversion results of the field data obtained from the SBI algorithm. (a) Inverted model with localized regularization adjustments for an initial location of x = 11 m and x = 17 m; z = 1.5 m and z = 7 m. (b) Inverted model with localized regularization adjustments for x = 12 m and x = 16 m; z = 1.5 m and z = 7 m after Flow 3. (c) Inverted model with localized regularization adjustments for x = 12 m and x = 16 m; z = 2 m and z = 7 m after Flow 4. bv = 10–1 is assigned for obtaining the models shown in Figure 9a–c. Black lines with double arrows indicate the horizontal location of the tunnel (x = 12.25–15.75 m) determined based on the blueprint, and the center is 14 m.

211x322mm (300 x 300 DPI)

This paper presented here as accepted for publication in Geophysics prior to copyediting and composition.
© 2025 The Authors. Published by the Society of Exploration Geophysicists.

Downloaded 02/13/25 to 130.54.130.252. Redistribution subject to SEG license or copyright; see Terms of Use at http://library.seg.org/page/policies/terms
DOI:10.1190/geo2024-0365.1

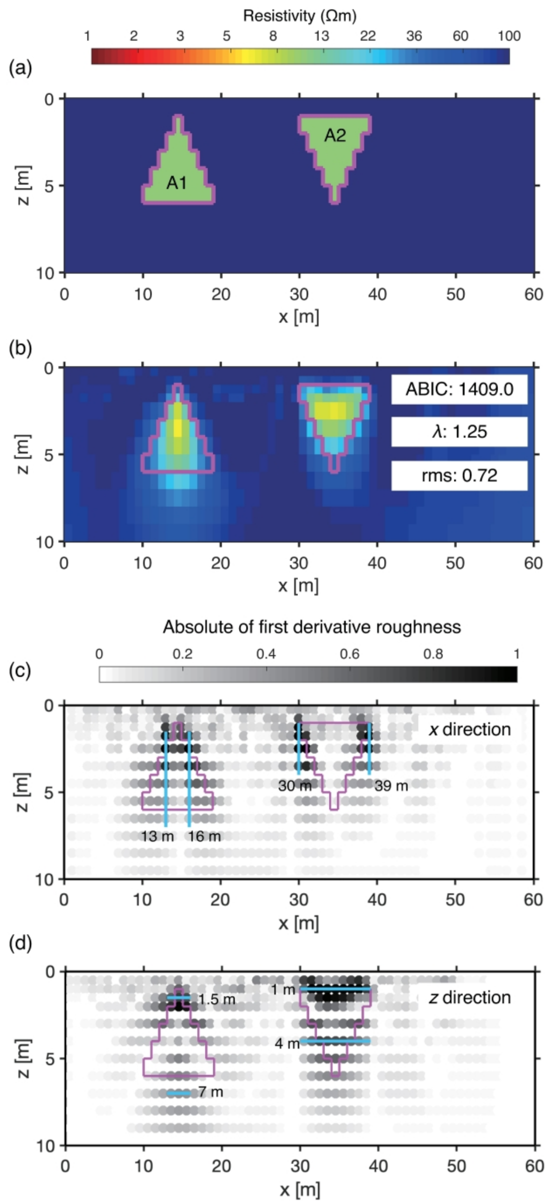

Figure 11. True model including the triangular structures, smooth inversion result, and its first-derivative roughness. (a) Two 10 Ωm triangular structures with upward and downward orientations (A1 and A2), are embedded in a 100 Ωm homogeneous half-space structure. (b) Inverted model using smoothness regularization. Magenta lines represent the true outline of the conductors. (c) and (d) present the absolute of the first-derivative roughness of the inverted model in (b) for the x- and z-directions, respectively. Light blue lines indicate our initial sharp boundary locations (A1: x = 13 m and x =16 m; z = 1.5 m and z = 7 m, and A2: x = 30 m and x =39 m; z = 1 m and z = 4 m).

212x418mm (300 x 300 DPI)

This paper presented here as accepted for publication in Geophysics prior to copyediting and composition.
© 2025 The Authors. Published by the Society of Exploration Geophysicists.

Downloaded 02/13/25 to 130.54.130.252. Redistribution subject to SEG license or copyright; see Terms of Use at http://library.seg.org/page/policies/terms
DOI:10.1190/geo2024-0365.1

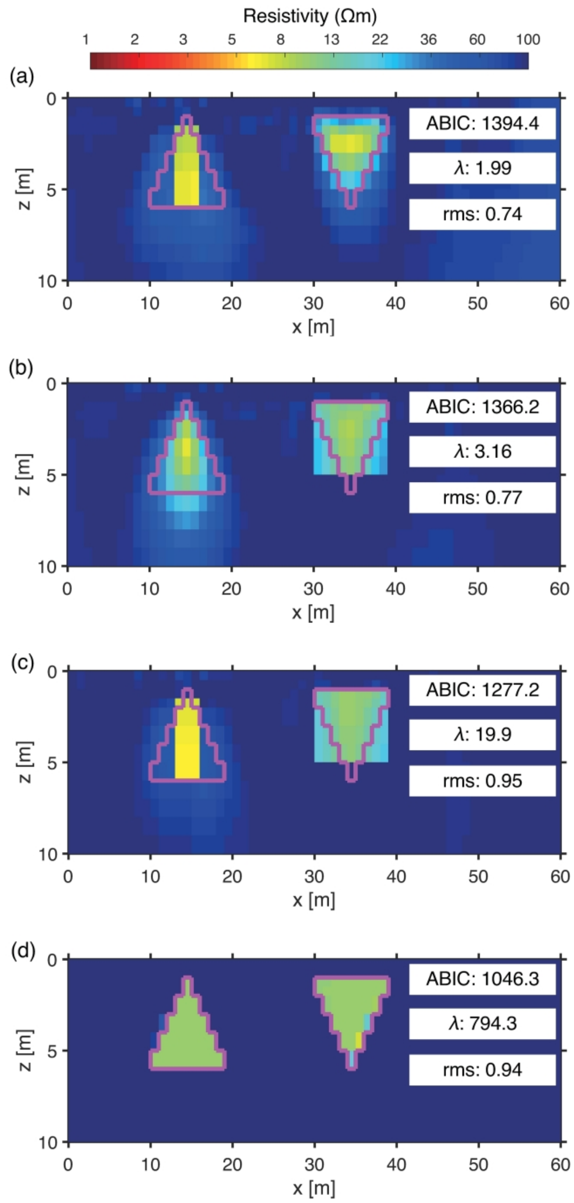

Figure 12. Inversion results of the synthetic data generated from the model, including the triangular structures (Figure 11a). Inverted models obtained by the SBI algorithm for (a) A1, (b) A2, and (c) both A1 and A2. (d) Inverted model with localized regularization adjustments for true sharp boundaries. The parameter bv was set to 10−1 to obtain the models depicted in Figure 11a and 11b, and to 10−2 in Figure 11c and 11d.

212x398mm (300 x 300 DPI)

© 2025 The Authors. Published by the Society of Exploration Geophysicists.

Downloaded 02/13/25 to 130.54.130.252. Redistribution subject to SEG license or copyright; see Terms of Use at http://library.seg.org/page/policies/terms
DOI:10.1190/geo2024-0365.1

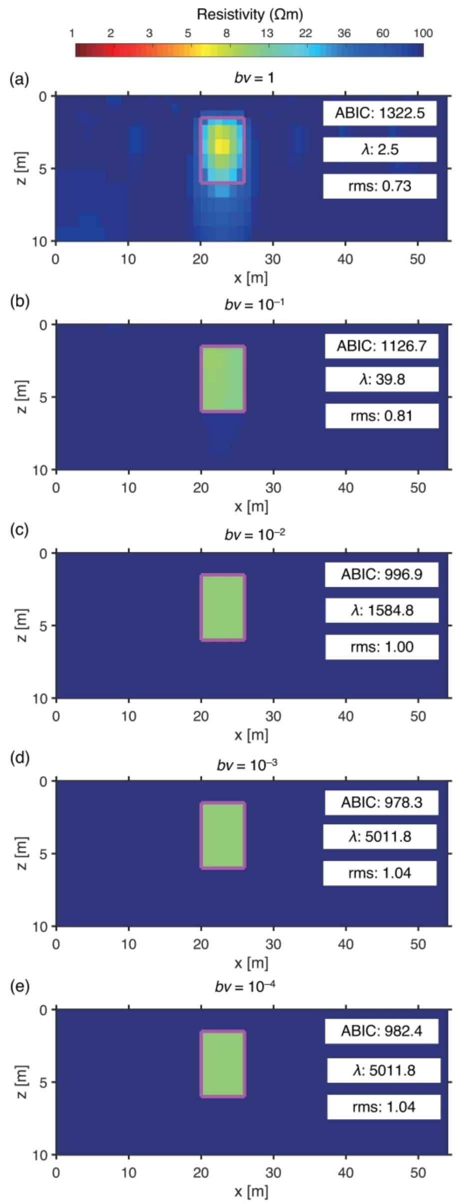

Figure A1. Inverted models obtained with bv ranging from 10–4 to 1 and localized regularization adjustments for x = 20 m and x = 26 m; z = 1.5 m and z = 6 m. bv = (a) 1, (b) 10–1, (c) 10–2, (d) 10–3, and (e) 10–4. Magenta lines represent the true outline of the conductor. (a) and (d) are the same for Figures 3a and 4c.

211x501mm (300 x 300 DPI)

© 2025 The Authors. Published by the Society of Exploration Geophysicists.

DATA AND MATERIALS AVAILABILITY

Data associated with this research are available and can be obtained by#xD;#xA;contacting the corresponding author.

Downloaded 02/13/25 to 130.54.130.252. Redistribution subject to SEG license or copyright; see Terms of Use at http://library.seg.org/page/policies/terms
DOI:10.1190/geo2024-0385.1

This paper presented here as accepted for publication in Geophysics prior to copyediting and composition.
© 2025 The Authors. Published by the Society of Exploration Geophysicists.